

**Key Points:**

- The El Niño-Southern Oscillation (ENSO), North Atlantic Oscillation, North Pacific Oscillation (NPO), and Southern Annular mode impacts on seasonal extreme wave heights are examined at global scale using altimeter and ERA5 reanalysis data
- Distinct seasonal and regional signatures of climate variability modes are observed in line with associated atmospheric circulation changes
- Possible combined influences of ENSO and NPO are first identified over the northeast North Pacific during boreal winter

**Supporting Information:**

- Supporting Information S1

**Correspondence to:**

S.-K. Min,  
[skmin@postech.ac.kr](mailto:skmin@postech.ac.kr)

**Citation:**

Patra, A., Min, S.-K., & Seong, M.-G. (2020). Climate variability impacts on global extreme wave heights: Seasonal assessment using satellite data and ERA5 reanalysis. *Journal of Geophysical Research: Oceans*, 125, e2020JC016754. <https://doi.org/10.1029/2020JC016754>

Received 31 AUG 2020  
Accepted 18 NOV 2020

## Climate Variability Impacts on Global Extreme Wave Heights: Seasonal Assessment Using Satellite Data and ERA5 Reanalysis

Anindita Patra<sup>1</sup>, Seung-Ki Min<sup>1</sup> , and Min-Gyu Seong<sup>1</sup>

<sup>1</sup>Division of Environmental Science and Engineering, Pohang University of Science and Technology, Pohang, Gyeongbuk, Korea

**Abstract** This study examines the influences of major climate variability modes on global extreme significant wave height (SWH) during 1992–2016 using merged satellite altimeter records and ERA5 reanalysis data set. El Niño-Southern Oscillation (ENSO), North Atlantic Oscillation (NAO), North Pacific Oscillation (NPO), and Southern Annular mode (SAM) are considered during December–February (DJF), March–May (MAM), June–August (JJA), and September–November (SON). A nonstationary generalized extreme value analysis is applied to seasonal maxima of SWH (Hmax) to identify the regions with significant impacts of climate variability. In addition to major impacts over the northeastern North Pacific (NP) and Maritime Continent during DJF, signature of ENSO in Hmax is observed over the southeast South Pacific during all seasons associated with the Pacific South America pattern and over the western NP during JJA and SON through the El Niño-East Asian teleconnection mechanism. Notable contribution of NAO to North Atlantic Hmax, resulting from north-south movement of storm track, is observed during DJF and MAM. Increased Hmax is concentrated around the northeast NP during the positive phase of NPO during DJF, which accompanies Aleutian low strengthening and suggests possible combined influence with ENSO. SAM influences on Hmax are characterized by a zonal pattern in the Southern mid- and high latitudes around the year, with seasonally distinct zonal extent and meridional shifts. Overall, the satellite and reanalysis data exhibit consistent results. Hmax responses are generally in accord with extreme wind and sea-level pressure gradient amplitude, supporting the wind-driven extreme wave mechanisms.

**Plain Language Summary** Extreme ocean wave heights exert a profound effect on coastal livelihoods and infrastructure and understanding their variabilities is fundamental to making reliable risk analysis. Large-scale climate variability modes like El Niño-Southern Oscillation (ENSO), North Atlantic Oscillation (NAO), North Pacific Oscillation (NPO), and Southern Annular mode (SAM) generate interannual variations in extreme ocean waves over different areas during different seasons. However, a comprehensive seasonal-specific assessment at global scale has not been conducted. Using satellite observations and reanalysis data, this study examines influences of these climate variability modes on seasonal extreme waves. In addition to its wintertime impact on northeast North Pacific, El Niño induces larger wave extremes over western North Pacific during boreal summer and autumn and lower wave extremes around southeast South Pacific all year round. The NAO drives the north-south dipole response over North Atlantic during winter and spring whereas the NPO makes a strong impact over the northeast North Pacific during winter with possible combined influences with ENSO. The seasonal variations in SAM affect extreme waves along different latitudes with different zonal extent. The response patterns of extreme waves instigated by these climate variability modes generally follow those of atmospheric teleconnection patterns.

### 1. Introduction

Waves exert stress on coastal structure, sediment transport, coastal erosion, and so on and are therefore an important contributor to coastal hazards. The coincidence of high waves and a high tide further augments coastal vulnerability. Waves are primarily driven by surface wind. Wave height increase associated with mean and extreme wind speed increase are well documented in literature (Young, 1999; Young & Ribal, 2019; Young et al., 2011, 2012). The historical trends of wave heights have been widely studied (Cox

& Swail, 2001; Gulev & Grigorjeva, 2004, 2006; Hemer et al., 2010; Patra & Bhaskaran, 2016, 2017; Semedo et al., 2011; Wang & Swail, 2001, 2002; X. L. Wang et al., 2012; Young et al., 2011). In addition, modes of interannual climate variability such as El Niño–Southern Oscillation (ENSO), North Atlantic Oscillation (NAO), Southern Annular mode (SAM) impose variability on atmospheric circulation and eventually on wind stress throughout the global ocean basin. Accordingly, the climate variability modes drive interannual global wave variability through impacting ocean–atmosphere interactions, winds, and storm activities (Bromirski et al., 2013; Dodet et al., 2010; Fan et al., 2012; Hemer et al., 2010; Semedo et al., 2011; Stopa et al., 2013; X. L. Wang & Swail, 2001). El Niño events lead to anomalously high erosion through wave forcing in the northeast Pacific while Southeastern Australia experiences increased erosion rates during La Niña (Barnard et al., 2015, 2017). As a major source of climate variability in the North Atlantic Ocean, NAO shows strong authority in driving wave power variability and trends over North Atlantic regions (Bromirski & Cayan, 2015). A strong correlation between wave climate and the SAM has been reported for the Southern Ocean (Hemer et al., 2010, 2013).

It is “extreme” wave which is crucial in affecting coastal infrastructure and environment (Hansom et al., 2015). Characteristic changes of extreme and mean waves are reported to be of different nature (Feng et al., 2012; Mori et al., 2010), probably associated with more frequent extreme events. There are, however, limited studies in the context of climate variability impacts on extreme waves at a global scale. Influences of climate variability modes on mean wave heights are well known but their impacts on extreme wave heights have not been widely identified due to the larger noise related to shorter time scales. Furthermore, simple linear regression analysis, typically used for mean variables, cannot be applied to extreme waves because of their nonnormality nature (Coles, 2001), and recent studies have employed the extreme value theory. Izaguirre et al. (2011) conducted a nonstationary Generalized Extreme Value (GEV) analysis for monthly maximum significant wave height (SWH) from merged satellite altimeter data set considering climate variability indices as an additive covariate of location parameter. Ten climate variability modes including ENSO, NAO, and SAM were analyzed to explore global teleconnection patterns in annual extreme wave heights, but seasonal contributions have not been assessed. Kumar et al. (2016) undertook a GEV analysis to inspect combined influence of ENSO and Pacific Decadal Oscillation (PDO) on extreme SWH using ERA-Interim and ERA-20C reanalyses during the boreal winter (December–February [DJF]). They focused on Northern Hemisphere variability in extreme SWH, and further examined its connection with variability in wind speed and sea-level pressure (SLP) gradient amplitude to highlight that atmospheric teleconnection pattern induces the extreme SWH changes. Using the same method and ERA-20C reanalysis, Kumar et al. (2019) examined seasonally distinct responses of extreme SWHs over the Indian Ocean to ENSO, SAM, and the Indian Ocean Dipole (IOD), finding the same physical mechanism at work.

The current study aims at investigating the impacts of the major modes of interannual climate variability on seasonal extreme SWH, using merged satellite altimeter datasets and ERA5 reanalysis for an extended period spanning 1992–2016. This study conducts a more comprehensive investigation of climate variability impacts on extreme waves worldwide than previous studies in several ways. First, we consider different seasons to understand seasonal-specific influences of climate variability on extreme waves. A nonstationary GEV analysis is performed for seasonal extremes in order to better capture the distinct teleconnection responses associated with each climate variability modes (Lim et al., 2016; Meneghini et al., 2007; Min et al., 2013). In particular, response patterns of wave climate to SAM are known to differ according to seasons and regions (Hemer et al., 2010; A. G. Marshall et al., 2018). There are distinct seasonal responses of SWH to certain indices over some regions. By analyzing annual extremes, it is difficult to specify which season the results correspond to. Therefore, seasonal analysis adds more clarity to explanation of spatial pattern as response of certain climate indices. For example, NAO is mostly active in DJF seasons, so studying NAO influence on DJF extreme is more meaningful than on annual extreme. It should be noted that, for tropical regions, the high-wave season does not have to be hemispheric winter, as the swells from the Southern Hemisphere are stronger than those from the Northern Hemisphere, plus there might be the impact of tropical cyclones. So, extreme SWH over this region (ENSO influence) is examined for all four seasons.

Second, in addition to ENSO, NAO, and SAM, the influence of North Pacific Oscillation (NPO) on extreme waves is examined, which has not been studied before. Also, combined influences of ENSO and NPO on extreme SWH are carried out for different combinations of ENSO and NPO phases. Third, we use new datasets

**Table 1**  
*A List of Previous Studies on Climate Variability Impacts on Wave Heights in Comparison With Current Study*

Reference	Data (period)	Variables	Climate variability	Analysis domains	Analysis methods
X. L. Wang and Swail (2001)	Wave model hindcast (1958–1997)	(Seasonal) 90th and 99th percentiles SWH, mean SLP	NAO	North Atlantic and the North Pacific	Linear trend, Redundancy analysis
Gulev and Grigorieva (2004)	Voluntary observing ship data (1958–2002)	Annual mean SWH (basin averaged)	NAO, NPI, SOI	Global Ocean	Linear trend
Gulev and Grigorieva (2006)	Voluntary observing ship data (1958–2002)	Seasonal mean SWH	NAO, NPI	North Atlantic and the North Pacific	Linear trend, EOF, canonical correlation analysis
Menendez et al. (2008)	Buoys (1985–2007)	98th percentile of 6-hourly SWH	ENSO, PNA, NPI	Northeast Pacific Ocean	Time-dependent GPD-Poisson model
Izaguirre et al. (2010)	Satellite altimeter (1992–2006)	Monthly maxima SWH	NAO, EA, EA/WR	Southern Europe	Time-dependent GEV
Hemer et al. (2010)	Satellite altimeter (1985–2006), ERA-40 (1980–2001)	Seasonal mean SWH	SAM, SOI	Southern Hemisphere	Linear trend, correlation map, EOF analysis
Izaguirre et al. (2011)	Satellite altimeter (1992–2010)	(Annual) extreme SWH	AO, SAM, ENSO, PNA, NAO, EA, EA/WR, SCA, DMI, QBO	Global Ocean	Nonstationary GEV
Stopa et al. (2013)	CFSR reanalysis (1979–2009)	Mean SWH	AO, AAO, ENSO, MJO	Global Ocean	EOF
Kumar et al. (2016)	ERA-Interim (1980–2014), ERA-20C (1952–2010)	(DJF) extreme SWH, wind speed, SLP gradient	ENSO, NAO, PDO	Northern Hemisphere	Nonstationary GEV, Composite analysis (ENSO and PDO)
Kumar et al. (2019)	ERA-20C (1957–2010)	Seasonal extreme SWH, wind speed, SLP	ENSO, IOD, SAM	Indian Ocean	Nonstationary GEV, Composite analysis (ENSO and IOD)
Current study	Satellite altimeter (1992–2016), ERA5 (1979–2018)	Seasonal extreme SWH, wind speed, SLP gradient	ENSO, NAO, NPO, SAM	Global Ocean	Nonstationary GEV, Composite analysis (ENSO and NPO)

Abbreviations: AAO, Antarctic Oscillation; AO, Arctic Oscillation; DJF, December–February; DMI, Dipole Mode Index; EA, East Atlantic Pattern; EA/WR, East Atlantic-Western Russia pattern; ENSO, El Niño–Southern Oscillation; IOD, Indian Ocean Dipole; MJO, Madden-Julian Oscillation; NAO, North Atlantic Oscillation; NPI, North Pacific Index; NPO, North Pacific Oscillation; PDO, Pacific Decadal Oscillation; PNA, Pacific North America index; QBO, QuasiBiennial Oscillation; SAM, Southern Annular Mode; SCA, Scandinavian index; SLP, sea-level pressure; SOI, Southern Oscillation Index; SWH, significant wave height.

that cover recent years, which will provide a way of testing robustness of the previous findings as well as newly obtained results. In particular, the use of new satellite datasets with updated calibration and quality control techniques applied provides improved confidence in altimeter data set in comparison to the previously used one (e.g., Izaguirre et al., 2011). Robustness of satellite-based results are further checked through comparison with those from the ERA5 reanalysis data set. Finally, similar to previous mechanism studies, response patterns of wind speed, SLP, and SLP gradient amplitude to climate variability are analyzed for different seasons to uncover the potential connection between atmospheric teleconnection patterns and SWH extremes. The novelty of the present study in view of previous relevant studies is detailed in Table 1.

The arrangement of the study is as follows. Section 2 describes data for extremes, climate indices, and methodology of GEV analysis. The response patterns of seasonal extreme SWH to each climate variability modes, along with combined influence of ENSO and NPO are detailed in Section 3 where underlying physical mechanism is also discussed. Conclusions are given in Section 4.

## 2. Data and Methods

### 2.1. Data

Satellite measurements are the only data set, other than numerical model outputs, which provides global scale wave heights. The primary data set used here for surface wind speed and SWH is the merged satellite altimeter records from nine altimeter missions, namely: ERS-1, TOPEX-Poseidon, ERS-2, GEOSAT Follow-ON, Jason-1, Jason-2, ENVISAT, Cryosat, and SARAL. The analysis period covers March 1992 to February 2017. The advantage of considering altimeter data is that coincident measurement of wind speed and SWH provides confidence in physical interpretation of analysis. Daily data files are sourced from public domain repositories of the French Research Institute for Exploitation of the Sea (<ftp://ftp.ifremer.fr/ifremer/cersat/products/swath/altimeters/waves>). Altimeter measurements were extracted from the various missions, then screened according to quality flag values, corrected using cross-platform and buoy comparison, and collected into homogeneous daily data files in order to provide long-term time series. A full description of the procedure involved in data screening and correction for each individual altimeter can be found in Queffelec and Croizé-Fillon (2017). In this study, calibrated and validated swath data files are downloaded and made into gridded files. To ensure enough satellite passes, daily individual swath measurements are aggregated into  $3^\circ$  longitude  $\times$   $2^\circ$  latitude grid boxes, and maximum value in the box is chosen. Seasonal block maxima of SWH (Hmax) and wind speed (Wmax) are then computed out of these daily maxima for each  $3^\circ \times 2^\circ$  grid box. There can be number of issues with extreme values from satellite observations. Altimeters are “nadir looking” instruments, therefore have a good spatial resolution along track, but low resolution across track. Another fact is that satellite has a repeat cycle of 10 days or more, so there is possibility for a single satellite to undersample small-size storms (Young & Ribal, 2019). However, collocating data over a  $3^\circ \times 2^\circ$  grid box from all the satellites helps to compensate for what may be missed when sampling at a single point. Wave height extremes from satellite records were used by several previous studies (Izaguirre et al., 2011; Takbash et al., 2019; Young et al., 2011, 2012). Takbash et al. (2019) have shown that, when compared to buoy data, the altimeter  $2^\circ \times 2^\circ$  product produces very similar extreme values. The usage of a larger grid ( $3^\circ \times 2^\circ$ ) and seasonal maxima rather than monthly further help in mitigating undersampling issue to a good extent.

The present study also uses ERA5 reanalysis data set to corroborate the results of altimeter data (<https://confluence.ecmwf.int/display/CKB/ERA5%3A+data+documentation>). ERA5 (C3S, 2017; <https://www.ecmwf.int/en/newsletter/159/meteorology/global-reanalysis-goodbye-era-interim-hello-era5>) is the most recent reanalysis product of the European Centre for Medium-Range Weather Forecasts with much higher spatial and temporal resolution than ERA-Interim (Dee et al., 2011). Key strengths of ERA5 compared to ERA-Interim include improved representation of troposphere, tropical cyclones, precipitation cycle, among others. ERA5 SWH and surface wind speeds ( $u_{10}$ ,  $v_{10}$ ) are extracted at every 6-h interval and have a horizontal resolution of  $0.5^\circ \times 0.5^\circ$  and  $0.25^\circ \times 0.25^\circ$ , respectively, for the complete available period (1979–2018). Furthermore, seasonal mean and maximum of SLP gradient amplitude (referred to as Gmean and Gmax, respectively), which represents geostrophic wind energy, are determined from 6-hourly ERA5 mean SLP data at  $0.25^\circ \times 0.25^\circ$  resolution. To ensure consistency with altimeter analysis, seasonal means and maxima are computed after collecting these data into  $3^\circ \times 2^\circ$  grid. When checking the main results of the spatial SWH response patterns to climate variability modes using data with  $0.5^\circ \times 0.5^\circ$  resolution, results remain the same (Figure S1), supporting that the use of  $3^\circ \times 2^\circ$  grid resolution is acceptable for analyzing large-scale patterns.

Takbash et al. (2019) argued that performance of reanalysis data set under extreme conditions is still limited. They mentioned that “the altimeter data show much greater fine scale structure, which is consistent with known tropical cyclone activity (not generally resolved by reanalysis model datasets).” Hodges et al. (2013) found that tropical cyclone intensities are underrepresented in the ERA-Interim reanalysis compared to the observations. The ERA5 data set is much improved than ERA-Interim including its higher spatial and temporal resolution. Nevertheless, ERA5 also has limitations for describing small-scale phenomenon such as tropical cyclones (<https://confluence.ecmwf.int/display/CKB/ERA5%3A+uncertainty+estimation>). Also, in reanalysis data set, the quantity of data assimilated into the models changes with time, possibly inducing temporal inhomogeneity (Aarnes et al., 2012, 2015; Breivik et al., 2013). Therefore, given that both datasets

have their own limitations, using both datasets and comparing results will increase confidence in the results of extreme analysis.

## 2.2. Climate Indices

As the major climate oscillations, ENSO, NAO, NPO, and SAM are considered here. ENSO, characterized by sea surface temperature anomaly across the tropical Pacific basin (Rasmusson & Carpenter, 1982), is a prominent coupled atmosphere-ocean phenomenon affecting global climate. To investigate ENSO impact, monthly Niño3.4 index (SST anomaly averaged over 5°S–5°N, 170°W–120°W, calculated based on ERSST.v5) was obtained from National Oceanic and Atmospheric Administration (NOAA)—Climate Prediction Center (CPC) (<https://www.cpc.ncep.noaa.gov/data/indices/ersst5.nino.mth.81-10.ascii>). The dynamics and teleconnections of ENSO are complex (e.g., Yeh, Cai, et al., 2018), so the results may depend on the choice of the index. In this respect, we use the Multivariate ENSO Index (MEI; Wolter & Timlin, 2011) which is known to better capture the larger ENSO pattern, which is obtained from NOAA (<https://psl.noaa.gov/enso/mei/>). In addition to SST, the MEI time series is derived using other meteorological fields like surface winds, SLP, and outgoing longwave radiation over the tropical Pacific basin (30°S–30°N and 100°E–70°W). The main ENSO analyses in the current study are presented based on Niño3.4 index, which are compared with the MEI-based ones. The NAO index, defined by the leading empirical orthogonal function (EOF) of 1,000 hPa geopotential height over the North Atlantic (NA), has strong signature over NA especially during winter (Hurrell, 1995; Hurrell & Van Loon, 1997; Hurrell et al., 2003). Monthly time series of normalized NAO is availed from NOAA-CPC ([ftp://ftp.cpc.ncep.noaa.gov/wd52dg/data/indices/nao\\_index.tim](ftp://ftp.cpc.ncep.noaa.gov/wd52dg/data/indices/nao_index.tim)). NPO, the analog of NAO in the North Pacific (NP) is computed through an EOF analysis which involves detrended DJF mean ERA5 SLP over the area of 0°–70°N and 120°E–120°W. The second principal component is defined as a NPO index following Linkin and Nigam (2008) and Paik et al. (2017). The SAM index representing north-south oscillation of low pressure surrounding Antarctica is obtained from the station-based index of G. J. Marshall (2003), based on difference in normalized monthly zonal SLP at 40°S and 65°S (<https://legacy.bas.ac.uk/met/gjma/sam.html>). The detrended and normalized seasonal averaged indices are used in GEV analysis (Figure 1).

## 2.3. Nonstationary GEV Analysis

Seasonal extremes at each defined grid are fitted into time-dependent GEV distribution following previous studies (Coles, 2001; Kharin & Zwiers, 2005; Kumar et al., 2016; Min et al., 2013; Zhang et al., 2010). Alternatively, extremes can be studied by applying the generalized Pareto distribution (GPD) to values exceeding a threshold, so-called a peaks-over-threshold (POT) method (Coles, 2001). Although GPD approach makes better use of the available data, choosing threshold for POT approach is critical. The fitting block maxima to GEV distribution is more straightforward. The GEV cumulative distribution function is expressed by

$$F(x; \mu_t, \sigma_t, \xi_t) = \begin{cases} \exp\left[-\exp\left(-\frac{x - \mu_t}{\sigma_t}\right)\right], & \xi_t = 0 \\ \exp\left[-\left(1 + \xi_t \frac{x - \mu_t}{\sigma_t}\right)^{-\frac{1}{\xi_t}}\right], & \xi_t \neq 0, \left(1 + \xi_t \frac{x - \mu_t}{\sigma_t}\right) > 0, \end{cases} \quad (1)$$

where  $\mu_t$ ,  $\sigma_t$ ,  $\xi_t$  are the location, scale, and shape parameters, respectively. As the altimeter records cover a short period, we perform a Kolmogorov-Smirnov test to ensure that wave extremes for this period are well fitted to GEV model using the method of maximum likelihood (Kharin & Zwiers, 2005). To inspect the influence of climate variability on seasonal extremes, a climate variability index  $\nu$  (ENSO, NAO, NPO, or SAM index in this study) is used as a covariate of GEV parameters. According to a likelihood ratio test (see below), impact of climate variability on extremes are found to occur mainly through location parameter with almost no influence of scale and shape parameters, consistent with previous studies (e.g., Kumar et al., 2016; Min et al., 2013). Therefore, we consider changes in location parameter with time ( $t$ ) as follows:

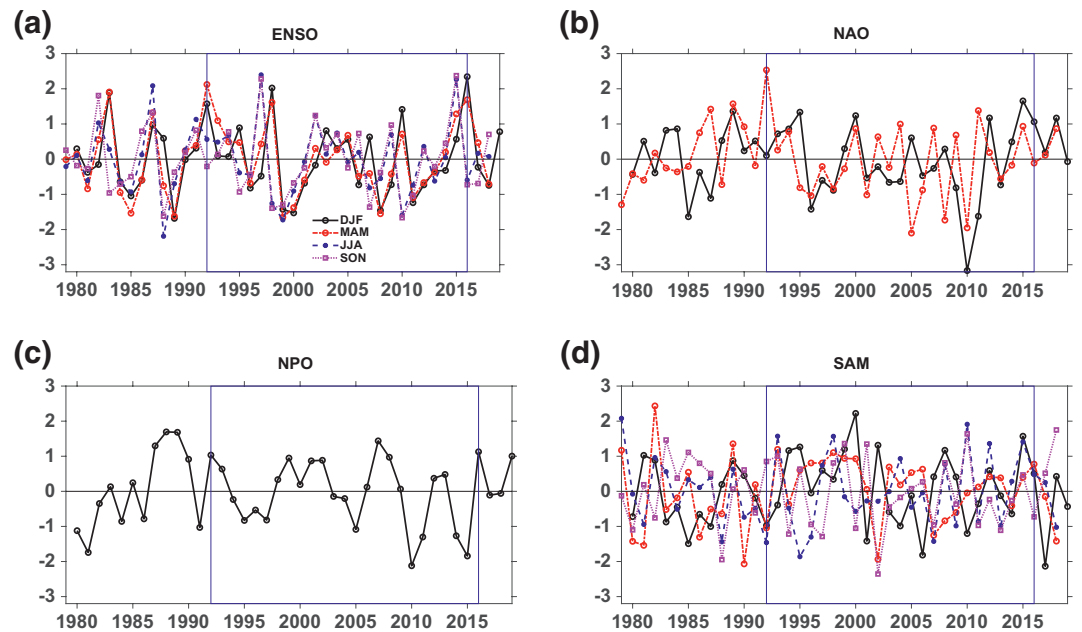


**Figure 1.** Seasonal mean time series of (a) Niño3.4, (b) NAO, (c) NPO, and (d) SAM indices during 1979–2018. All time series are detrended and normalized based on 1979–2018. Light blue boxes indicate the common analysis period of 1992–2016 based on the availability of altimeter data. DJF season of a year considers January–February of that year and December of previous year, which makes Niño3.4 series in DJF shifted by 1 year compared to those in JJA and SON, following the seasonal evolution of ENSO.

$$\mu_t = \mu_0 + \mu_1(v_t - v_0) \quad (2)$$

where  $v_t$  and  $v_0$  are climate variability index at time  $t$  and  $t_0$ , respectively,  $\mu_0$  is the location parameter at time  $t_0$ , and  $\mu_1$  is the regression coefficient quantifying relationship between climate variability and location parameter. Climate variabilities make GEV distribution to shift right or left through variations in location parameter. Statistical significance of the influence of climate variability is determined through a likelihood ratio test which compares the log likelihood between a nonstationary GEV and a stationary GEV model (Kharin & Zwiers, 2005).

The GEV analysis is conducted for Hmax, Wmax, and Gmax on grid base and the spatial distribution of resulting regression coefficient of location parameter (Equation 2) is drawn to examine the overall response patterns to individual climate variability modes. The response patterns of SLP mean and Gmean are also compared, which are obtained based on simple linear regression. For NAO and NPO, high-energetic winter (and spring for NAO) season of the respective hemispheres are considered. For ENSO and SAM, large variability remains across the year, so we consider all four seasons: DJF, March–May (MAM), June–August (JJA), and September–November (SON). The following results are based on positive phase of each climate variability mode.

### 3. Results

#### 3.1. ENSO Influence

ENSO, characterized by anomalous sea surface temperatures in the eastern equatorial Pacific, is a major climate phenomenon of much of the tropics and subtropics. The influence of ENSO on DJF Hmax and Wmax during 1992–2016 is displayed in Figure 2, which show the spatial distribution of the regression coefficients of GEV location parameters for Hmax and Wmax ( $\mu_1$  in Equation 2) onto the DJF Niño3.4 index as described in Section 2.3. Significant positive responses of altimeter extremes are noticed over the northeastern North Pacific (NENP), intertropical convergence zone (ITCZ), and South Pacific convergence

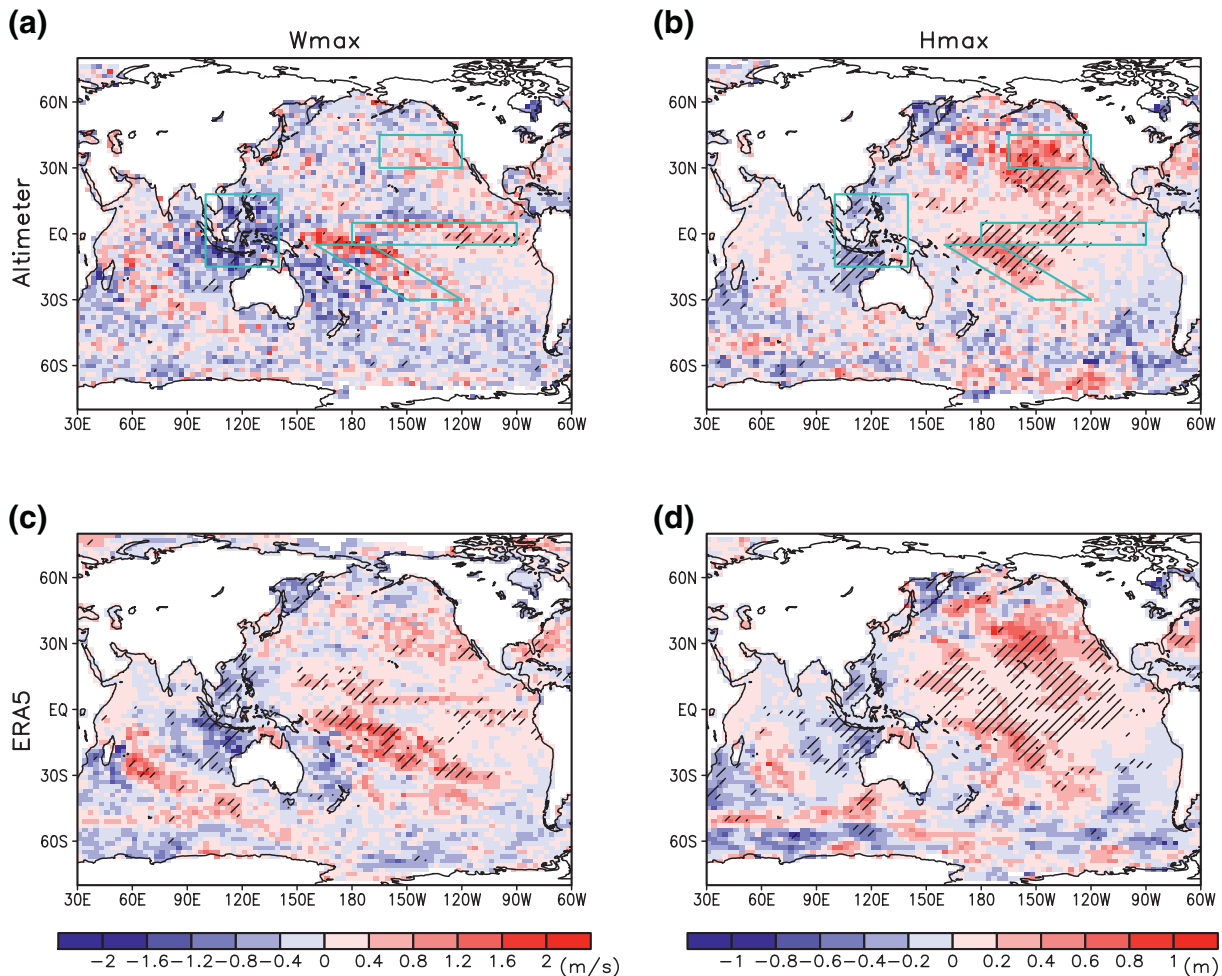


**Figure 2.** ENSO influence on DJF extremes over Indo-Pacific Ocean: (a) altimeter wind speed, (b) altimeter SWH, (c) ERA5 wind speed, and (d) ERA5 SWH. Spatial distributions of the regression coefficients of GEV location parameters onto Niño3.4 index are displayed, which are obtained based on Equation 2 for 1992–2016. Hatching represents regions with significance influences at 10% level. Cyan boxes in (a and b) indicate the four selected regions with significant ENSO influences.

zone (SPCZ) during El Niño (Figures 2a and 2b). However, opposite responses are found over the coastal regions of western NP and Maritime Continent. This agrees with the finding of Kumar et al. (2016) based on ERA-Interim and ERA-20C datasets for a different period. The overall patterns of Hmax and Wmax variability in ERA5 (Figures 2c and 2d) resemble those from altimeter observations, which remain almost the same when considering a longer period of 1979–2018 (Figure S1). Good agreement of ENSO responses between altimeter observations and reanalysis products indicates robustness of our results. On the other hand, wave height intensification during El Niño over the Tasman Sea, reported by Izaguirre et al. (2011), cannot be seen during DJF. A similar change occurs in JJA (see Figure 4 below), supporting the previous finding with a response season specified.

During El Niño events, anomalous low pressure persists over the eastern Pacific extending from northern high latitudes to subtropical south and anomalous high pressure over the tropical western, southeastern Pacific and Indian Ocean (Figure 3a). Consequently, SLP gradient amplitude is increased around the NENP, ITCZ, and SPCZ; and is decreased over the Maritime Continent and southeastern South Pacific (Figure 3b). A similar spatial pattern observed in Gmax (Figure 3c) enforces alike variability in wind speed extremes and further in wave height extremes. Area averaged response amplitude for four significantly impacted areas (Figure 3d) clearly depicts the interrelation between Gmax, Wmax, and Hmax. The warm temperature anomalies of tropical eastern Pacific would lead to more frequent and intense storms by strengthening

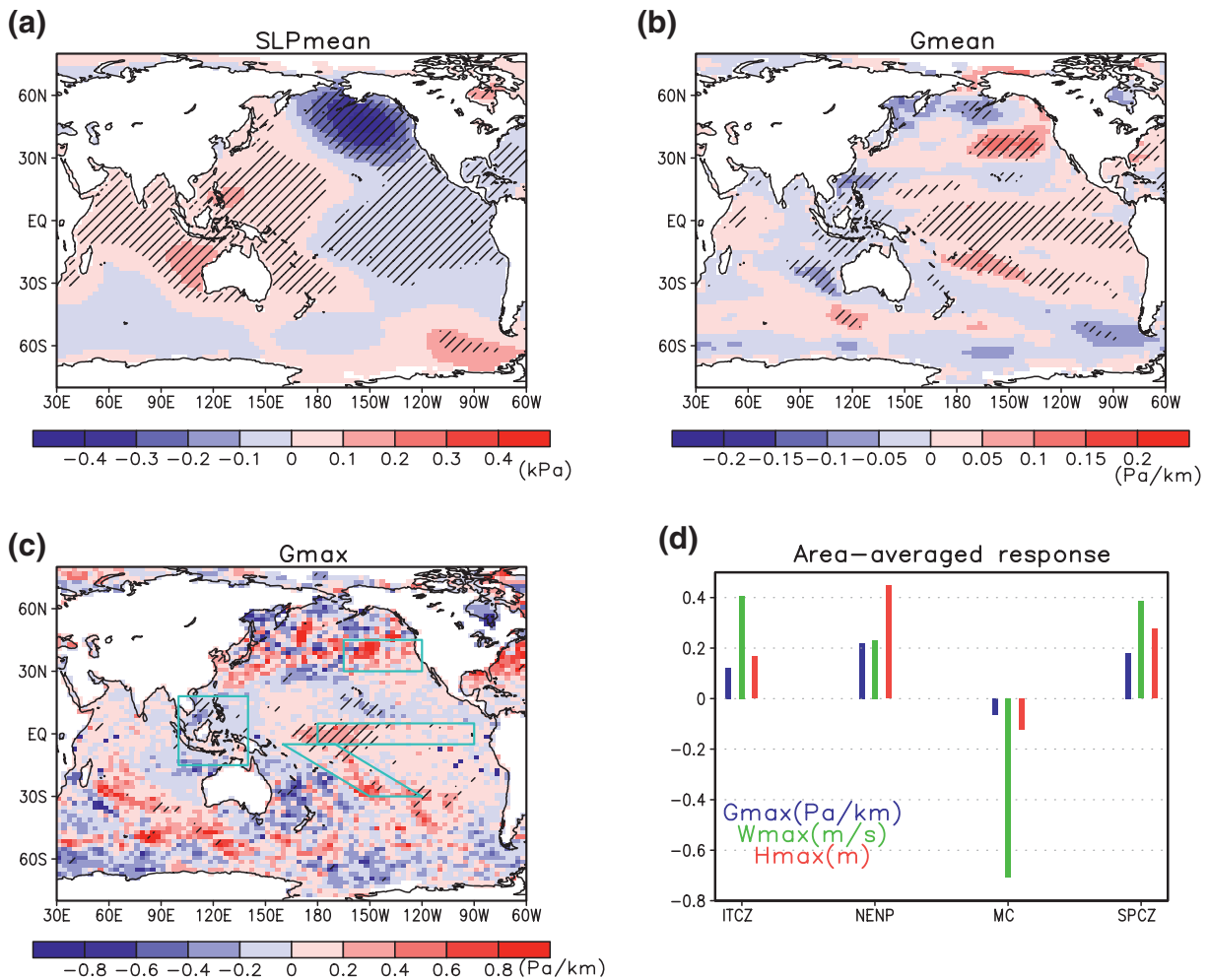


**Figure 3.** ENSO influence on DJF (a) mean SLP, (b) mean SLP gradient amplitude, (c) extreme SLP gradient amplitude over Indo-Pacific Ocean, and (d) area averaged responses for four selected regions for 1992–2016 (cyan boxes in [c], Hmax and Wmax from altimeter, and Gmax from ERA5). Mean SLP and SLP gradient responses indicate regression coefficients onto Niño3.4 index based on simple linear regression. Hatching represents regions with significance influences at 5% level for seasonal mean and at 10% level for extremes.

instability. A strong relation of El Niño events and more frequent and intense Eastern Pacific tropical cyclones was reported by Jin et al. (2014). On the other hand, colder and dryer ocean surface with reduced storm activity results in less intense extremes along the coast of western NP and Maritime Continent (Power et al., 1999; B. Wang et al., 2000). Heightened wave activity over the SPCZ can be attributed in part to increased tropical cyclone activity over this region (Kuleshov et al., 2008; Vincent et al., 2011).

Seasonal variation in extreme wave response pattern to ENSO is illustrated in Figure 4. Significant ENSO influences persist year-round and vary in the spatial extent from season to season. A strong El Niño influence can be seen over western North Pacific during JJA and SON. It is well known that during boreal summer, tropical cyclone activity over the western North Pacific (WNP) is influenced by El Niño events (Camargo & Sobel, 2005; Chen & Lian, 2018). B. Wang and Zhang (2002) found the deepening of East Asian trough and the intensification and more frequent northward shift of the storm tracks over WNP during the fall of El Niño development years. The El Niño-East Asian teleconnection amplifies low-level cyclonic shear anomalies and the number of northward recurving tropical storms increases significantly. In MAM, noticeable increase of extremes prevails over ITCZ, but lower in amplitude than DJF.

Significantly higher wave height extremes occur in all seasons over southeastern South Pacific during La Niña years (negative responses in the figure corresponds to increases during La Niña years), more

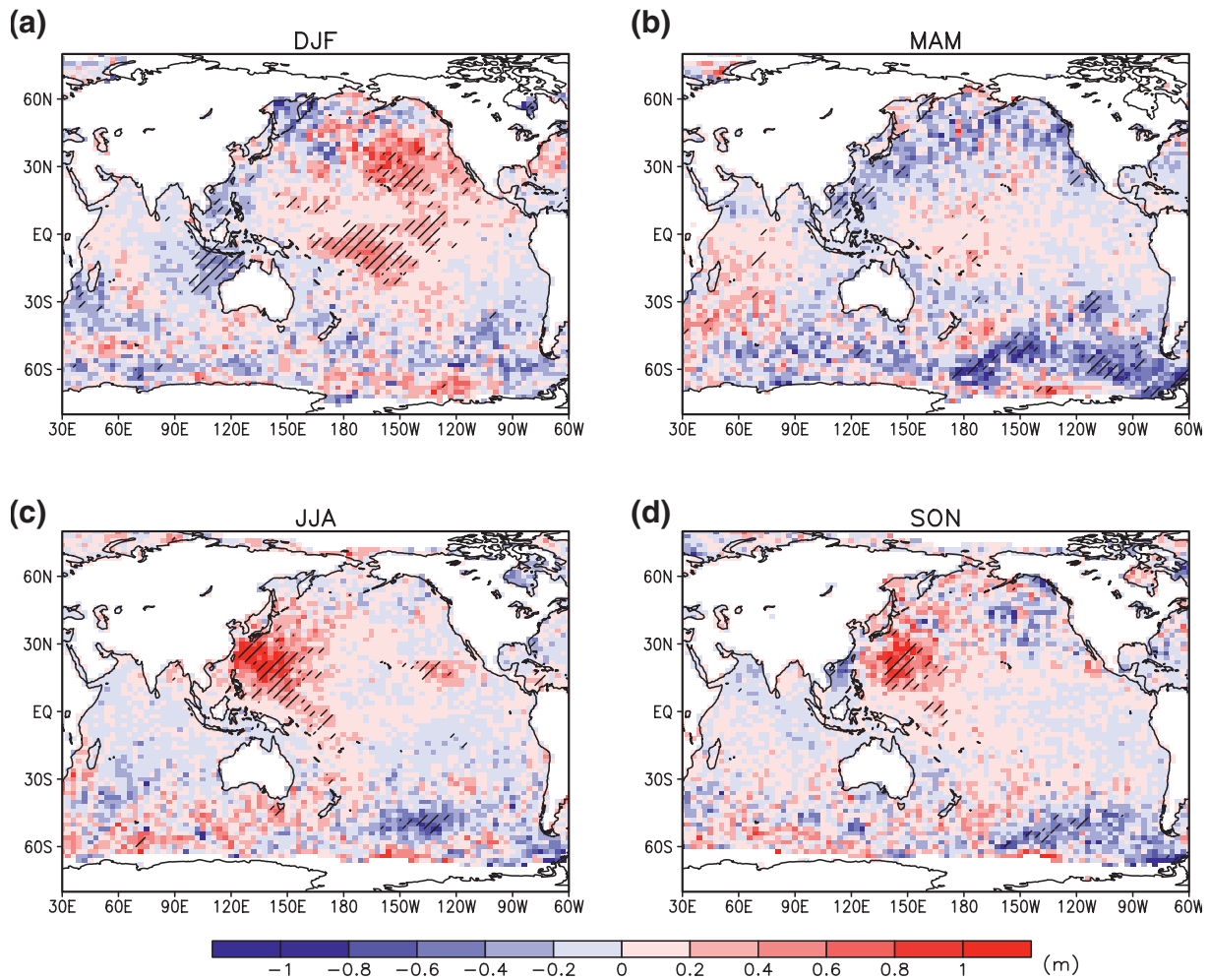


**Figure 4.** ENSO influence on Altimeter SWH extremes (1992–2016) over Indo-Pacific Ocean: (a) DJF (same as Figure 2b and shown again for comparison), (b) MAM, (c) JJA, and (d) SON. The regions with statistically significant responses at 10% level are hatched.

strongly during MAM. This is likely to be related with Pacific South America (PSA) mode which appears as response to tropical Pacific SST anomaly associated with ENSO. Spatial pattern of PSA mode is a zonally symmetric pattern with a phase reversal between high and midlatitudes, seen in the geopotential height anomalies (Mo & Paegle, 2001). Similar zonal patterns are evident in the SLP regression results for all seasons (figure not shown). The response pattern of Gmax (Figure S2) highlights La Niña-induced increase in wave extremes over southeastern South Pacific throughout the year, and El Niño-induced remarkable elevation of SWH extremes over WNP during JJA and SON. The increases in SWH extremes are evident over ITCZ in all seasons with a maximum in DJF. These implies that ENSO exerts seasonally distinct impacts on extreme wave heights by modulating atmospheric circulations over tropics and subtropics.

Additionally, influences of ENSO on extreme waves are analyzed using the MEI index (instead of Niño3.4). The Niño3.4 and MEI time series closely follow each other during the analysis period and correlation coefficients are close to 1 for all seasons (Figure S3). The high correlation between Niño3.4 and MEI was also reported by Wolter and Timlin (2011) and seems to be associated with high-quality SST data during the recent period. The seasonal response patterns using MEI index (Figure S4) are found very similar to those of Niño3.4 (Figure 4). There are few minor differences. For example, lesser number of grids experiences a significant negative response to MEI than to Niño3.4 over southeastern South Pacific during MAM.

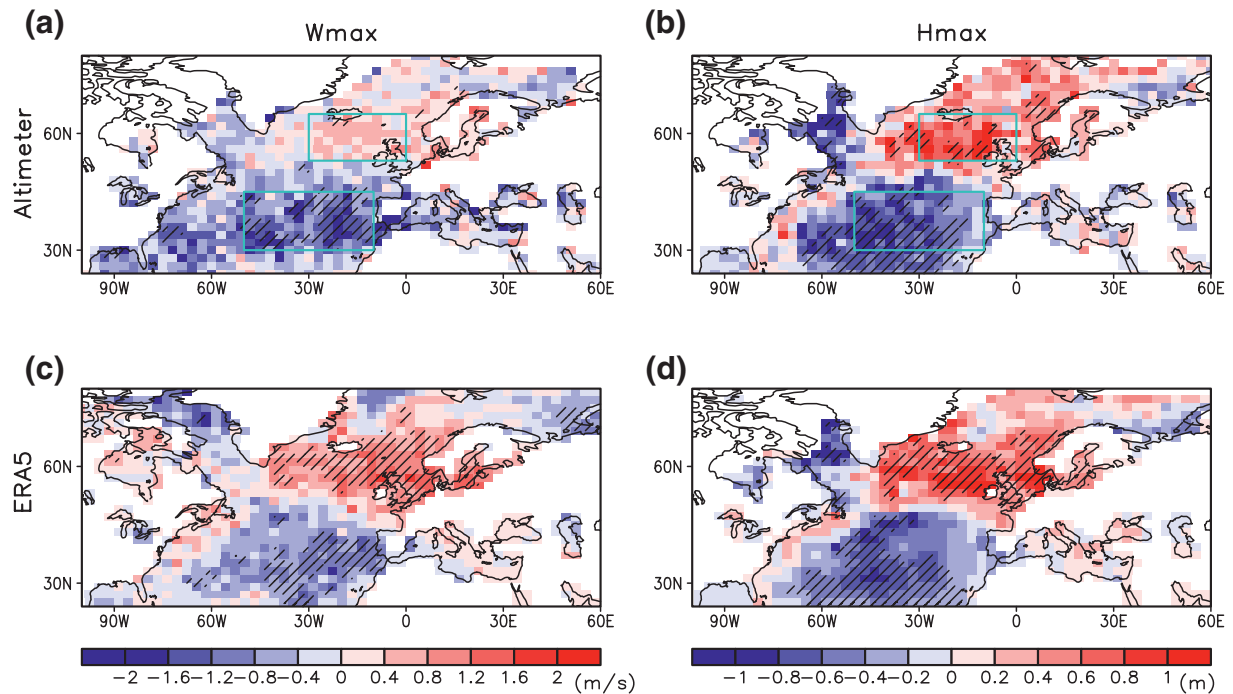


**Figure 5.** Same as Figure 2 but for NAO influence on DJF extremes: (a) altimeter wind speed, (b) altimeter SWH, (c) ERA5 wind speed and (d) ERA5 SWH. Cyan boxes indicate two selected regions (Iceland and Azores) with significant influences of NAO.

### 3.2. NAO Influence

The NAO, characterized by a meridional dipole pattern of anomalous pressure, is known since long to affect climate variability over the NA during northern winter months (Hurrell, 1995; Hurrell & Van Loon, 1997; Hurrell et al., 2003; Santo et al., 2015). Spatial patterns of DJF wind and SWH extremes associated with positive NAO are illustrated in Figure 5. Significant strengthening of wave height and wind extremes are seen north of 45°N poleward with a center located near the western coasts of Ireland and Scotland during the positive phase of NAO, reaffirming previous studies (Bromirski & Cayan, 2015; Gleeson et al., 2017). Equal level of weakening is found south of 40°N focused around the southeast NA to westward. Altimeter and ERA5 exhibit essentially same results, which are overall consistent with the previous findings (Izaguirre et al., 2011; Kumar et al., 2016; X. L. Wang & Swail, 2001). Noticeable is the marginal impact on the US east coast, as also reported by Bromirski and Cayan (2015) and Semedo et al. (2011).

In addition to Hmax and Wmax, this study provides mechanistic insight into the observed SWH variability. Regression pattern of SLP onto NAO reveals anomalous low pressure north of 60°N poleward and high pressure south of that over the NA during the positive phase of NAO (Figure 6a). As a result, winter mean SLP gradient sharpens due to strengthening of the Icelandic Low and Azores High (Figure 6b). In a similar way, Gmax has been altered over the NA (Figure 6c), thereby enhancing the westerlies that generate larger waves over the northeast NA. This is also suggestive of intense extreme waves associated with NAO in the Baltic Sea (Mentaschi et al., 2017). Heightened extreme waves during positive NAO winters are also related to movement of the jet stream, and therefore the storm track, toward the west coast of Ireland (Gleeson et al., 2019). Contrarily, significant increase in number of cyclones over the Azores region during negative NAO winters is responsible for increased wave heights there (Andrade et al., 2008). Figure 6d summarizes opposite responses of extreme waves to positive NAO and responsible mechanisms over Iceland and Azores regions. Our GEV analysis confirms that the impact of NAO is much less over the US east coast than European coast. Boreal spring shows a similar response of Hmax to the DJF case but with much reduced magnitude (Figure S5). Summer season variability (figure not shown) does not follow the pattern of increases seen in winter, reflecting a reduced effect of NAO during summer (Bromirski & Cayan, 2015).

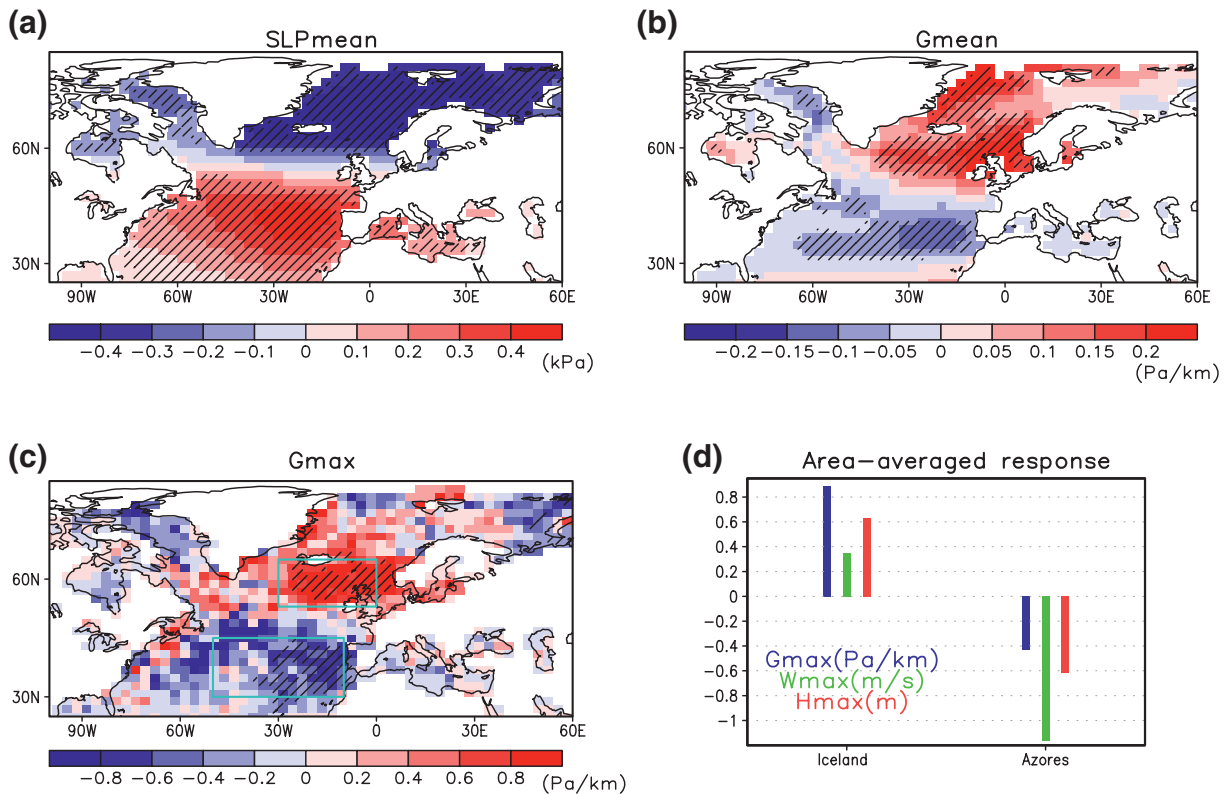


**Figure 6.** Same as Figure 3 but for NAO influence on DJF (a) mean SLP, (b) mean SLP gradient amplitude, (c) extreme SLP gradient amplitude, and (d) area averaged responses over two regions with significant responses (Iceland and Azores).

### 3.3. NPO Influence

In a similar way to NAO for the North Atlantic Ocean, NPO is a representative climate variability mode accompanying anomalous pressure patterns in the North Pacific Ocean. It is signaled by a large-scale meridional dipole in SLP and latitudinal movements of jet streams (Linkin & Nigam, 2008). Though several studies examined NAO influence, NPO influence on extreme waves has not been studied before. Results from a GEV analysis with NPO present greater DJF wave extremes over the eastern North Pacific centered around northeast during its positive phase (Figure 7). This is accompanied by reduced wave extremes over the central western North Pacific Ocean (CWNP) and the Sea of Okhotsk, indicating the increased extreme waves during the negative phase (also see Figure S1b). The impact of NPO on surface temperature, winds, and subsequently on sea ice over the Sea of Okhotsk was reported by Paik et al. (2017). In comparison to Hmax, significant Wmax increase is limited only to the NENP. Altimeter and ERA5 data set are in accordance with each other in depicting variability associated with NPO.

Positive NPO is defined by an eastward shifted and enhanced Aleutian low pressure and a high pressure over a large region in the central NP (Rogers, 1981). SLP regression pattern with NPO during DJF indeed exhibits the deepening of Aleutian low and the increase of high pressure to the south (Figure 8a). Moreover, it agrees with the eastward shift of center of the southern lobe of the SLP in the NPO after mid-1990s (Yeh, Yi, et al., 2018). While regressing SLP gradient amplitude onto the NPO index, a tripole pattern is identified in the NP with a strong increase over the NENP, a decrease over the CWNP, and an increase to the south (Figure 8b). Interestingly, accordant response of Gmax is discerned from GEV analysis (Figure 8c), apparently explaining about evolution of wind speed and eventually wave height extremes. Area mean responses show that NENP region associated with Aleutian low experiences stronger changes in extremes than the CWNP region. NPO, like its counterpart NAO in the Atlantic, is characterized by northeastward shift of the Asian-Pacific jet stream and associated storm track displacement during its positive phase (Lau, 1988). Extremes have diminished to its south owing to subdued storm activity, which will be opposite during its

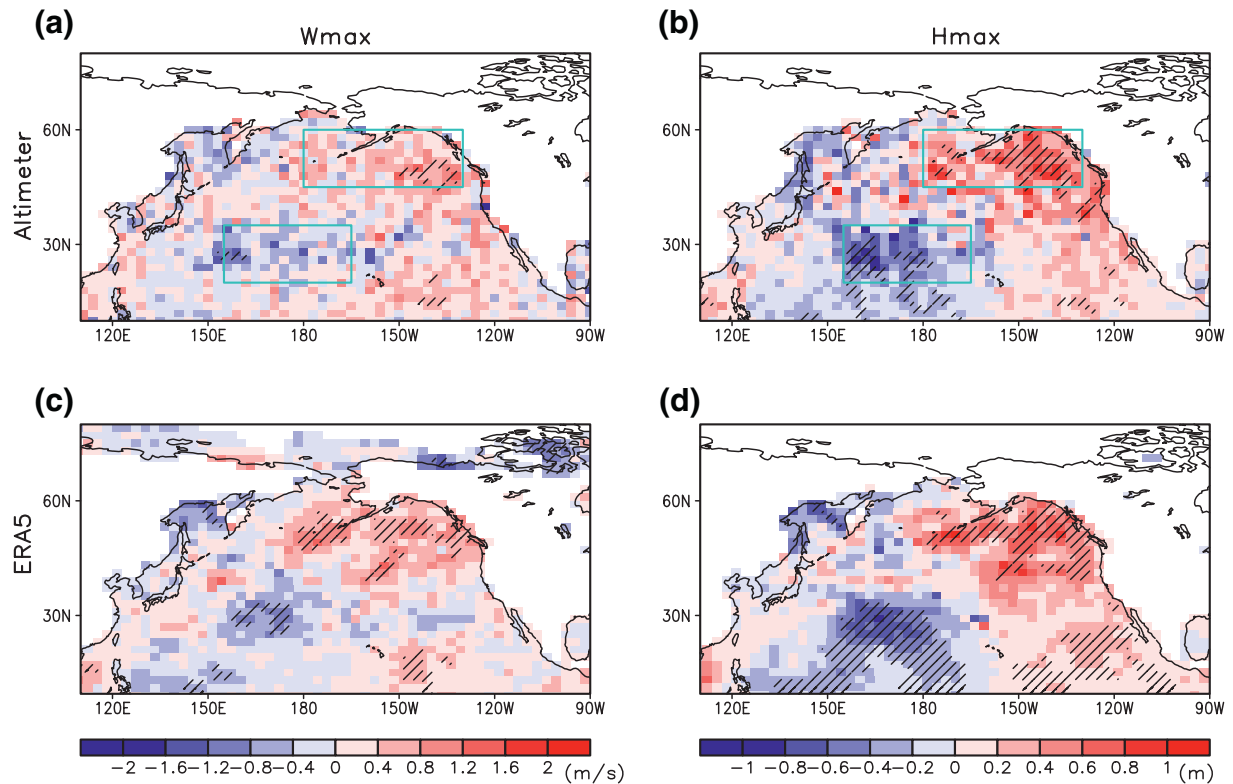


**Figure 7.** Same as Figure 2 but for NPO influence on DJF extremes: (a) altimeter wind speed, (b) altimeter SWH, (c) ERA5 wind speed, and (d) ERA5 SWH. Cyan boxes in (a and b) indicates two selected regions of significant influence of NPO: northeastern North Pacific (NENP) and central western North Pacific (CWNP).

negative phase of NPO. Noteworthy is that despite their resemblance, NAO is much more effective to induce climate variability than NPO (Linkin & Nigam, 2008).

### 3.4. Combined Influence of ENSO and NPO

There might be possible ENSO/NPO combined effect over the NENP which gets affected by both variability modes. Although the number of sample years is limited, combined influence of ENSO and NPO is worth discussing, which has not been examined before. Sensitivity tests show that there are no prominent differences when using a NPO index independent of ENSO (figure not shown), which is obtained based on a linear regression (cf. Min et al., 2013). This result reflects a weakened relationship between NPO and ENSO after mid-1990s (Yeh, Yi, et al., 2018). Nevertheless, we examine combined ENSO/NPO influences during DJF by carrying out a composite analysis for different combinations of ENSO and NPO phases. Here the years for different ENSO/NPO combinations (Table 2) are selected based on a threshold of  $\pm 0.5$  standard deviation of each variability index. Composite patterns of mean SWH ( $H_{avg}$ ) anomalies for different ENSO/NPO combinations are compared in Figure 9. During the in-phase years like El Niño/NPO+ (La Niña/NPO-),  $H_{avg}$  trends to increase (decrease) more strongly around the NENP and central tropical Pacific Ocean while it decreases (increases) over the western coastal NP and CWNP. In contrast, the years when ENSO and NPO are out of phase reveal weaker responses in  $H_{avg}$  due to the cancellation of individual mode's influences. For El Niño/NPO+ years, composite anomalies of SLP (Figure S6) demonstrate remarkable deepening of Aleutian low and high pressure along subtropical NP. The eastern Pacific anomalous low pressure associated with El Niño is strongly altered due to the presence of NPO. The exact opposite response is seen for La Niña/NPO- years. When the two modes are out of phase, SLP anomalies over the Aleutian regions become comparatively weak.  $H_{max}$  composites show similar results as those of  $H_{avg}$  but with stronger amplitude (figure not shown). When conducting the same composite analysis using MEI index,

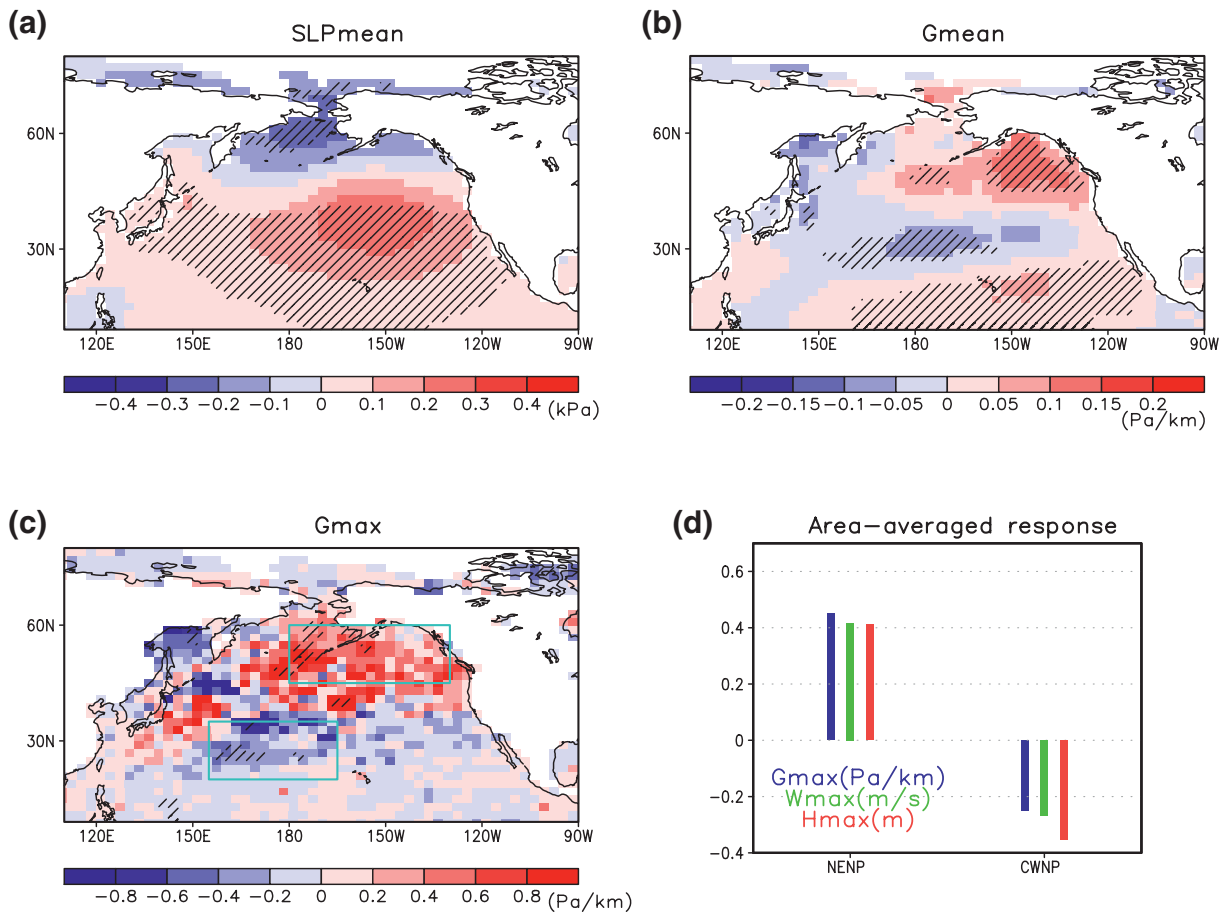


**Figure 8.** Same as Figure 3 but for NPO influence on DJF (a) mean SLP, (b) mean SLP gradient amplitude, (c) extreme SLP gradient amplitude, and (d) area averaged responses for two hotspot regions (NENP and CWNP, defined in Figure 7).

composite characteristics remain similar to those from Niño3.4 (Figure S7), indicating the insensitivity to the use of different ENSO index. Small variation in magnitude can be seen due to slight changes in selected years for different ENSO-NPO combinations (Table S1). The changes in selected years particularly occur for mild ENSO years (normalized index close to 0.5), not for the strong ENSO years. Overall, NPO and ENSO can affect each other by modulating the other mode's influence on mean and extreme SWHs, for which further investigation of detailed physical mechanisms is warranted.

### 3.5. SAM Influence

The SAM index is the dominant recurring and persistent large-scale pattern of the Southern Ocean pressure anomalies. Figure 10 shows the spatial pattern of SAM influence on JJA Hmax and Wmax over the Southern Hemisphere. The positive phase of SAM enhances extreme wave height significantly over the Pacific and Indian sections of Southern Ocean with a peak over around 60°S (Figures 10b and 10d), which is in line with the analysis of Izaguirre et al. (2011) using monthly extremes all year round. Strong positive correlation of SAM and JJA mean SWH over this area is also reported by previous studies (Hemer et al., 2013; A. G. Marshall et al., 2018). Hemer et al. (2013) stated that the limited influence on the Atlantic section of Southern Ocean is due to the shadowing effect of the South American continent as it blocks storm systems from propagating

**Table 2**

*Selected Years (DJFs) for Different Combinations of ENSO and NPO Phases Using Thresholds of ±0.5 Standard Deviation of Each Variability Index (Detrended and Normalized During 1992–2016)*

	El Niño (ENSO+)	La Niña (ENSO–)
NPO+	2007, 2016	1999, 2001, 2008
NPO–	1995, 2005, 2010, 2015	1996, 2011

Abbreviations: DJF, December–February; ENSO, El Niño–Southern Oscillation; NPO, North Pacific Oscillation.

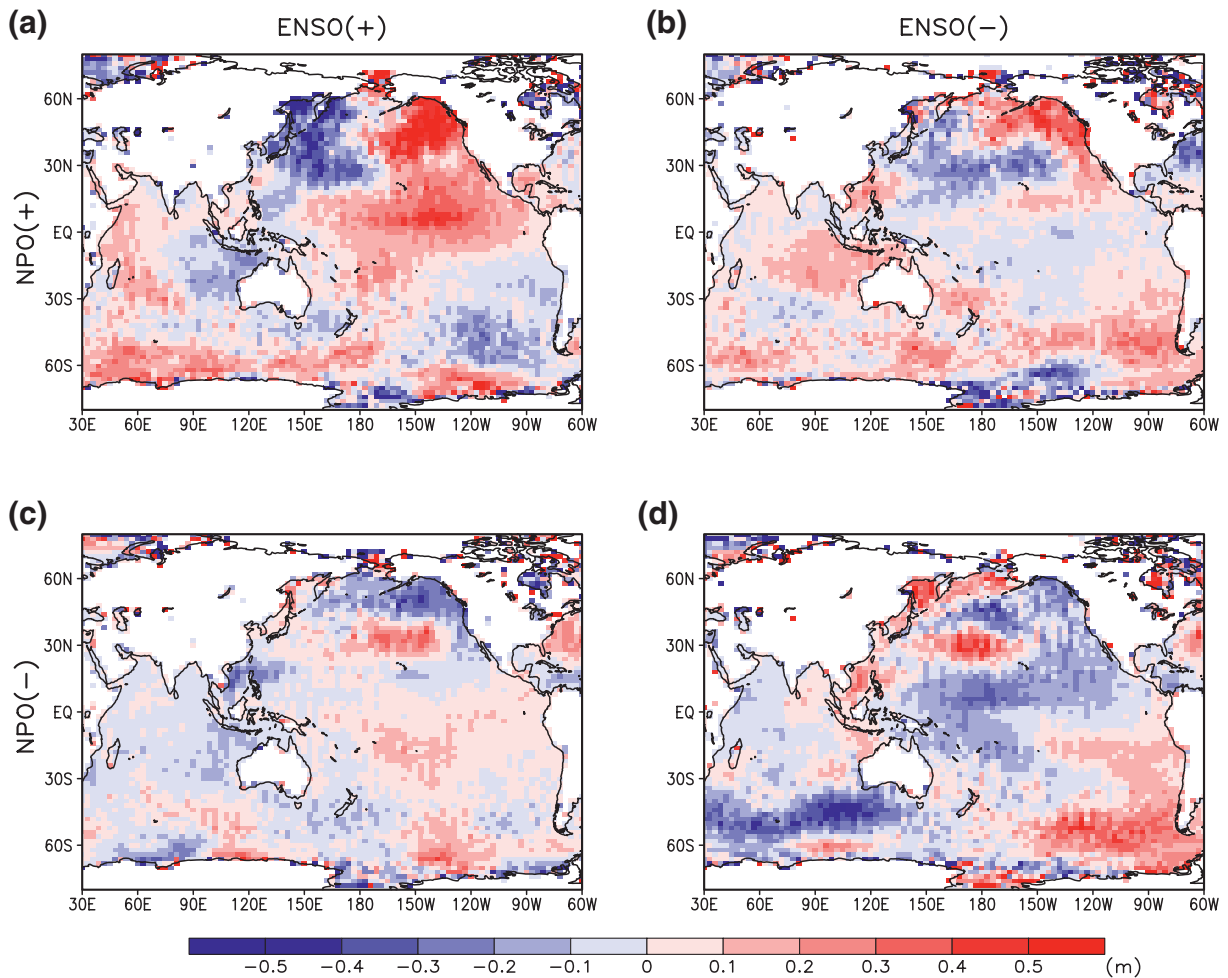


**Figure 9.** Composite patterns of DJF mean SWH (m) anomalies for the different combinations of ENSO and NPO: (a) El Niño/NPO+, (b) La Niña/NPO+, (c) El Niño/NPO–, and (d) La Niña/NPO– years (see Table 2) from ERA5 data set. Years for each case are selected as those with greater than  $\pm 0.5$  standard deviation based on detrended and normalized DJF mean ENSO and NPO time series during 1992–2016 (Figure 1).

around the southern latitudes. The positive phase of SAM brings reduced Hmax around 40°S over the South Atlantic, South Indian, and South Pacific Oceans in patches. The decreased wave activity over the South Pacific was not evident in the analysis of Izaguirre et al. (2011), but is clearly seen in the current seasonal analysis from both altimeter and reanalysis data. Wmax response patterns to SAM are well matched with those of Hmax (Figures 10a and 10c), suggesting its physical link with interannual variability in Hmax. The agreement in patterns of wind speed and wave height extremes, from both observation and reanalysis datasets, increases confidence in these response patterns.

Wind speed, and thereafter wave height, is a manifestation of atmospheric circulation pattern. The positive phase of SAM is characterized by a large low pressure anomaly around Antarctica and a belt of high pressure anomalies at midlatitudes. Regression pattern of mean SLP onto the SAM index during JJA shows amplification of low and high pressures around high latitudes and midlatitudes, respectively (Figure 11a). As a consequence, SLP gradient amplitude is intensified around 50°S–70°S but is reduced around 30°S–50°S (Figure 11b). Correspondingly, Gmax increases in the Indian and Pacific sections of Southern Ocean and decreases around midlatitudes of global ocean (Figure 11c). This explains the mechanism by which extreme winds and wave heights change in concert over the same region. Response of the above variables changes phase around 50°S–55°S (Figure 11d) such that zonal mean SLP response becomes from negative to positive toward north and vice versa for extreme Gmax, Wmax, and Hmax. It is very clear from the zonal mean response how SLP gradient drives wind speed and thereby wave height.

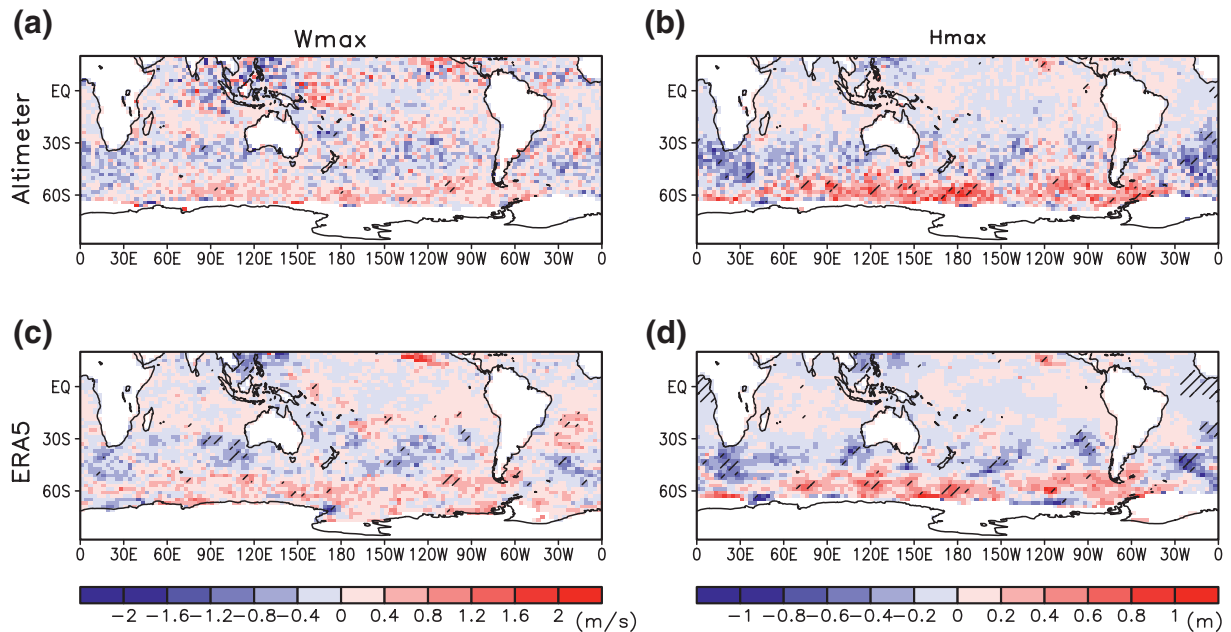


Figure 10. Same as Figure 2 but for SAM influence on JJA extremes: (a) altimeter wind speed, (b) altimeter SWH, (c) ERA5 wind speed, and (d) ERA5 SWH.

During DJF, wave responses to SAM in high latitudes is more widespread zonally than in JJA including the Atlantic section of Southern Ocean, unlike during JJA (Figure 12). On the other hand, midlatitude influences are more limited with almost no negative signal observed over South Pacific. Noteworthy is the fact that zonal center of the midlatitude influence is more poleward in DJF than JJA, particularly over the southeastern Indian Ocean. The meridional shift in the location of peak westerlies between DJF and JJA is associated with seasonal shift of the subtropical ridge (A. G. Marshall et al., 2018). Similarly, a poleward shift of the dry

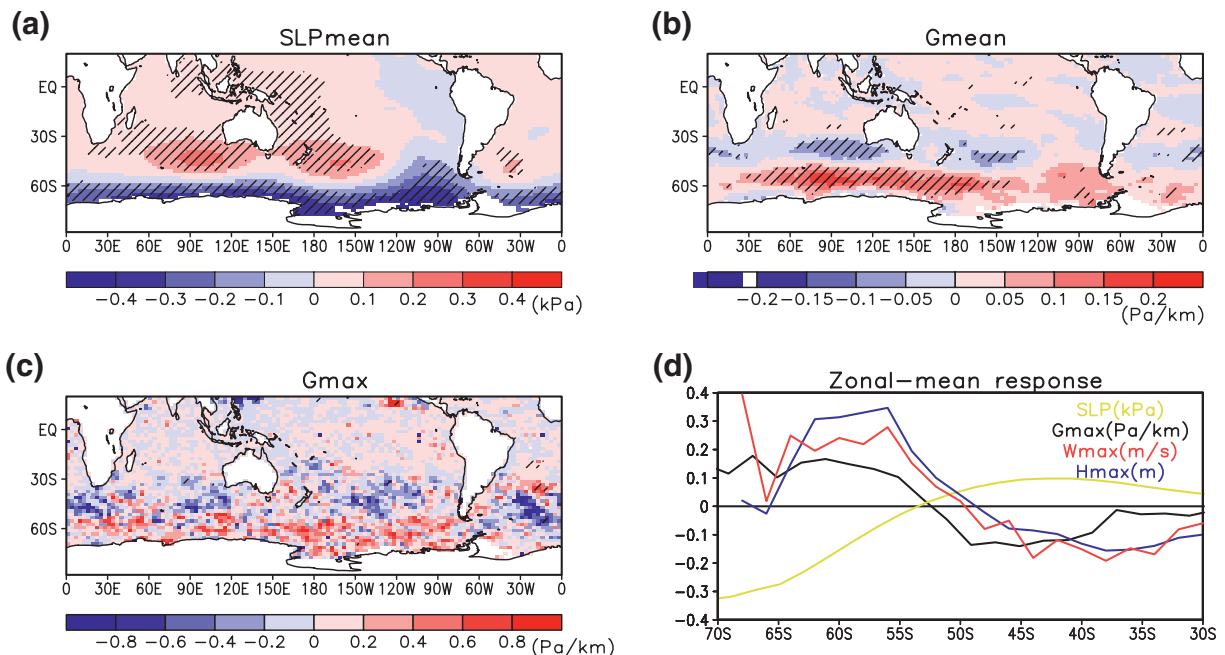
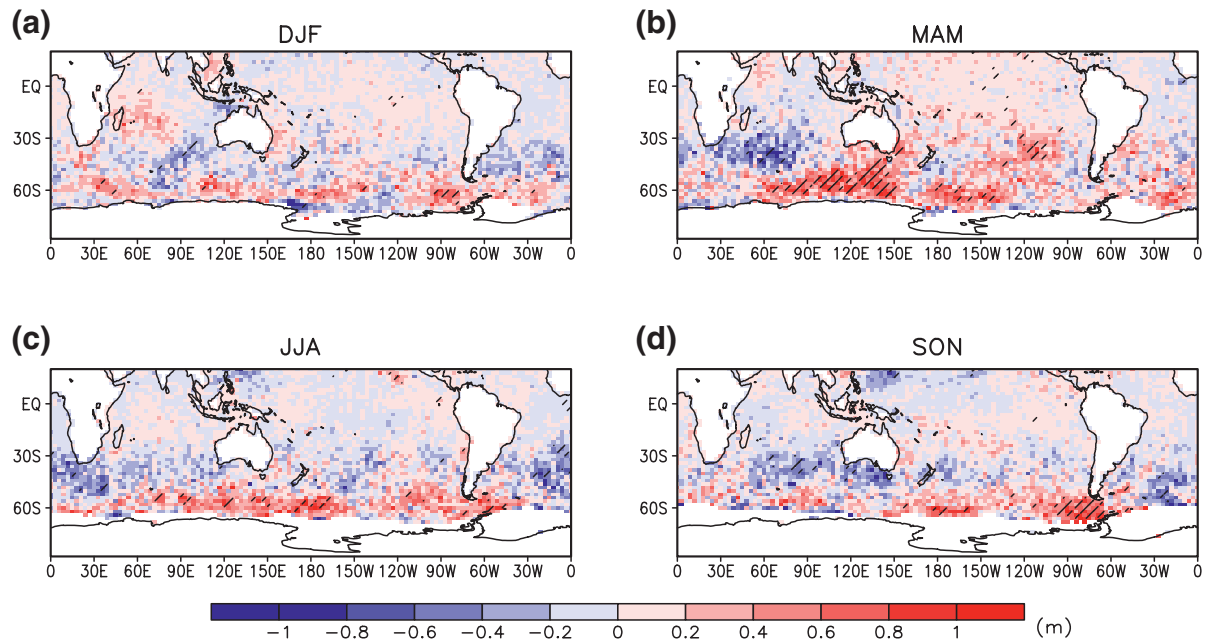


Figure 11. Same as Figure 3 but for SAM influence on JJA (a) mean SLP, (b) mean SLP gradient amplitude, (c) extreme SLP gradient amplitude, and (d) zonal mean responses (Hmax and Wmax from altimeter and SLP and Gmax from ERA5).



**Figure 12.** Same as Figure 4 but for SAM influence on SWH extremes (1992–2016): (a) DJF, (b) MAM, (c) JJA (same as Figure 10b and shown again for comparison), and (d) SON.

zone associated with positive SAM in DJF, as compared to JJA, is reported by Lim et al. (2016), who showed that covariability of SAM and ENSO regulate rainfall in austral summer. In this respect, when examining SAM influence on wave height extremes after removing ENSO based on a linear regression, there is no prominent differences in Hmax responses (figure not shown), which is also reported by Kumar et al. (2019) for Indian Ocean. A. G. Marshall et al. (2018) also emphasized that SAM, independent of ENSO, provides predictive signals for mean SWH and wind speed over the Northern Hemisphere extratropics during DJF. However, this connection is not observed from the current analysis. Associated responses in SLP, Gmean, and Gmax and their interconnection during DJF are consistent with the patterns of Hmax (Figure S8), supporting the physical mechanism as discussed in JJA.

Significant influence of SAM on wave extremes is detected throughout the year (Figure 12). In general, zonal structure of SAM with positive at high latitudes and negative at midlatitudes exist year-round, which shifts meridionally across seasons. For instance, southwest coast of Australia receives low wave extremes during JJA and SON, but not during other seasons. In all seasons, low pressure anomalies at high latitudes and high pressure anomalies at midlatitudes persist during positive SAM (A. G. Marshall et al., 2018), which is observed in Gmax (Figure S9). A notable feature is an intrusion of high-latitude positive signal to midlatitude over eastern South Pacific especially MAM and JJA, which cannot be seen in the corresponding Gmax pattern (Figure S9). This suggests that Southern Ocean swell may approach to eastern Pacific Ocean from southwest direction. The anticlockwise rotation of swells results in elevated wave extremes around Tasmania coast during these seasons. A. G. Marshall et al. (2018) have shown meridional component of wave energy propagating from high latitudes to midlatitudes, as westerly swell propagates along the great circle.

#### 4. Conclusions

The study provides an updated and detailed examination of the impacts of natural climate variability modes (ENSO, NAO, NPO, and SAM) on extreme SWH based on merged satellite altimeter and ERA5 reanalysis data set during 1992–2016. In particular, seasonal responses of extreme SWH are evaluated, which have not been studied comprehensively. Also, results from altimeter and reanalysis datasets are systematically compared to provide more confident results, considering different advantages and limitations between the two datasets. To identify areas with significant responses, a nonstationary GEV analysis is applied on

seasonal extremes using a given climate variability mode as a covariate to the location parameter of GEV distribution. In addition, response patterns of wind speed, SLP, and SLP gradient amplitude to climate variability modes are evaluated to elucidate underlying physical mechanisms which induce such interannual variability in wave extremes.

Each climate variability mode exerts distinct seasonal influences on extreme SWH across the globe, which are found to be associated with corresponding changes in atmospheric circulation and wind speed. During El Niño events, the intensification of SLP gradient explains increased wave extremes around the NENP, ITCZ, and SPCZ regions in DJF season, whereas the western NP and Maritime Continent exhibit opposite responses. Seasonal variability of ENSO response reveals high-wave extremes over WNP during JJA and SON, as El Niño-East Asian teleconnection influences tropical storm activity over this region. In all seasons, negative impact occurs around southeast South Pacific, resembling PSA mode which indicates ENSO teleconnection response in the Southern Hemisphere. It is worth noting that different types of ENSO, that is, Eastern-Pacific (EP) and Central-Pacific (CP) ENSO, may have different effects on the extreme wave climate through their distinct physical processes (Kao et al., 2009; Yeh, Cai, et al., 2018). In this respect, SST-based Niño3.4 index is limited and subsurface temperature indices can be more effective for detecting the two types of ENSO (e.g., Yu et al., 2011). This advocates future studies on the role of ENSO types in determining extreme wave responses using different ENSO indices.

The strengthening of Icelandic low associated with positive NAO enhances the westerlies and shifts storm tracks toward the west coast of Ireland, leading to larger wave extremes over the northeast North Atlantic during winter and spring, with almost no impact during summer. The positive phase of NPO, characterized by eastward shifted and enhanced Aleutian low, triggers northeastward shift of the Asian-Pacific jet stream and storm track, which produces greater wave extremes over the northeast NP during DJF. A composite analysis suggests that NPO can modify the influence of ENSO in the NP and vice versa in accordance to their relative phase and strength.

Antarctic low pressure trough deepens during positive SAM phase, resulting in poleward shifted and intensified wind band, and consequently larger ocean waves along the entire Southern Ocean around the year. Moreover, the impact of SAM on extremes shows strong seasonality in the response patterns with extended zonal extent and poleward shift during austral summer compared to winter. The eastern South Pacific experiences wave impacts from Southern Ocean swells during MAM and JJA.

Overall strong similarity between altimeter observations and ERA5 reanalysis support robustness of our results in spite of a short analysis period. This is partly due to the consideration of same spatial scales between two datasets, by applying aggregation into  $3^\circ \times 2^\circ$  grid boxes. Resulting clear signals of climate indices on the extreme wave climate indicate the weak influence of undersampling in satellite data. If the poor spatio-temporal coverage of altimeter data, in any case, is not enough to form statistically stable extreme values, the results would have been extremely noisy. Nevertheless, the undersampling issue of satellite data needs to be considered with care. Also, it should be noted that ERA5 reanalysis and altimeter observations are not completely independent because some satellite data have been assimilated into ERA5 reanalysis.

Our improved understanding of SWH response patterns will help to predict coastal impacts such that identified areas for greater extremes can be anticipated to have aggravated consequences. Our results have important implications for climate model evaluations as well as future extreme wave projections. Recently, long-term trends of extreme wave energy flux are suggested to be associated with long-term tendencies of ENSO, SAM, and NAO indices (Mentaschi et al., 2017). Climate projections of the 21st century indicate intensification of these indices under increased anthropogenic activity, which will likely induce intensified shift in wave extremes having adverse consequences on shoreline stability. This suggests that identified seasonal hotspot regions for each climate variability by the current study might face elevated wave extremes in the future. Reguero et al. (2019) also showed that global wave power is closely connected to ocean warming and thus can be identified as a proxy for climate change. In this respect, further studies are warranted on future changes in extreme wave heights with considering future changes in climate variability modes. Furthermore, future studies can be taken up considering other climate variability modes and their interrelations, which may affect extreme waves for different regions and seasons, including the Pacific North America teleconnection pattern, the Madden-Julian Oscillation, IOD, PDO, the Atlantic Multidecadal Oscillation, and so on (Table 1).

### Data Availability Statement

We acknowledge European Centre for Medium-Range Weather Forecasts for production of ERA5 reanalysis data set (<https://confluence.ecmwf.int/display/CKB/ERA5%3A+data+documentation>) and IFREMER (<ftp://ftp.ifremer.fr/ifremer/cersat/products/swath/altimeters/waves>) for making merged satellite altimeter records available.

### Acknowledgments

This study was supported by the National Research Foundation of Korea (NRF) grant funded by the Korea government (MSIT) (No. 2017R1A2B2008951) and the Korea Meteorological Administration Research and Development Program under Grant KMI2020-01413.

### References

Aarnes, O. J., Abdalla, S., Bidlot, J.-R., & Breivik, Ø. (2015). Marine wind and wave height trends at different ERA-Interim forecast ranges. *Journal of Climate*, 28, 819–837. <https://doi.org/10.1175/JCLI-D-14-00470.1>

Aarnes, O. J., Breivik, Ø., & Reistad, M. (2012). Wave extremes in the northeast Atlantic. *Journal of Climate*, 25, 1529–1543. <https://doi.org/10.1175/JCLI-D-11-00132.1>

Andrade, C., Trigo, R. M., Freitas, M. C., Gallego, M. C., Borges, P., & Ramos, A. M. (2008). Comparing historic records of storm frequency and the North Atlantic Oscillation (NAO) chronology for the Azores region. *The Holocene*, 18, 745–754. <https://doi.org/10.1177/0959683608091794>

Barnard, P. L., Short, A. D., Harley, M. D., Splinter, K. D., Vitousek, S., Turner, I. L., et al. (2015). Coastal vulnerability across the Pacific dominated by El Niño/Southern Oscillation. *Nature Geoscience*, 8(10), 801–807. <http://dx.doi.org/10.1038/ngeo2539>

Barnard, P. L., Hoover, D., Hubbard, D. M., Snyder, A., Ludka, B. C., Allan, J., et al. (2017). Extreme oceanographic forcing and coastal response due to the 2015–2016 El Niño. *Nature Communications*, 8(1). <https://doi.org/10.1038/ncomms14365>

Breivik, Ø., Aarnes, O. J., Bidlot, J.-R., Carrasco, A., & Sætra, Ø. (2013). Wave extremes in the northeast Atlantic from ensemble forecasts. *Journal of Climate*, 26, 7525–7540. <https://doi.org/10.1175/JCLI-D-12-00738.1>

Bromirski, P. D., & Cayan, D. R. (2015). Wave power variability and trends across the North Atlantic influenced by decadal climate patterns. *Journal of Geophysical Research: Oceans*, 120, 3419–3443. <https://doi.org/10.1002/2014JC010440>

Bromirski, P. D., Cayan, D. R., Helly, J., & Wittmann, P. (2013). Wave power variability and trends across the North Pacific. *Journal of Geophysical Research: Oceans*, 118, 6329–6348. <https://doi.org/10.1002/2013JC009189>

Camargo, S. J., & Sobel, A. H. (2005). Western North Pacific tropical cyclone intensity and ENSO. *Journal of Climate*, 18, 2996–3006. <https://doi.org/10.1175/JCLI3457.1>

Chen, D., & Lian, T. (2018). Interaction of western-Pacific tropical cyclones with El Niño diversity. *National Science Review*, 5, 803–804. <https://doi.org/10.1093/nsr/nwy126>

Coles, S. G. (2001). *An introduction to statistical modeling of extreme values* (p. 225). London, UK: Springer-Verlag.

Copernicus Climate Change Service (C3S). (2017). *ERA5: Fifth generation of ECMWF atmospheric reanalyses of the global climate* Copernicus Climate Change Service Climate Data Store (CDS), April 15, 2019. Retrieved from <https://cds.climate.copernicus.eu/cdsapp#!/home>

Cox, A. T., & Swail, V. R. (2001). A global wave hindcast over the period 1958–1997: Validation and climate assessment. *Journal of Geophysical Research*, 106, 2313–2329. <https://doi.org/10.1029/2001JC000301>

Dee, D. P., Uppala, S. M., Simmons, A. J., Berrisford, P., Poli, P., Kobayashi, S., et al. (2011). The ERA-Interim reanalysis: configuration and performance of the data assimilation system. *Quarterly Journal of the Royal Meteorological Society*, 137(656), 553–597. <https://doi.org/10.1002/qj.828>

Dodet, G., Bertin, X., & Taborada, R. (2010). Wave climate variability in the North-East Atlantic Ocean over the last six decades. *Ocean Modelling*, 31, 120–131. <https://doi.org/10.1016/j.ocemod.2009.10.010>

Fan, Y., Lin, S.-J., Held, I. M., Yu, Z., & Tolman, H. L. (2012). Global ocean surface wave simulation using a coupled atmosphere–wave model. *Journal of Climate*, 25, 6233–6252. <https://doi.org/10.1175/JCLI-D-11-00621.1>

Feng, X., Tsimplis, M., & Yelland, M. (2012). *Extreme waves at the polar front of North Atlantic from 2000 to 2009* (p. 5719). EGU General Assembly 2012, Vienna, Austria.

Gleeson, E., Clancy, C., Zubiate, L., Janjić, J., Gallagher, S., & Dias, F. (2019). Teleconnections and extreme ocean states in the Northeast Atlantic Ocean. *Advances in Science and Research*, 16, 11–29. <https://doi.org/10.5194/asr-16-11-2019>

Gleeson, E., Gallagher, S., Clancy, C., & Dias, F. (2017). NAO and extreme ocean states in the Northeast Atlantic Ocean. *Advances in Science and Research*, 14, 23–33. <https://doi.org/10.5194/asr-14-23-2017>

Gulev, S. K., & Grigorieva, V. (2004). Last century changes in ocean wind wave height from global visual wave data. *Geophysical Research Letters*, 31, L24302. <https://doi.org/10.1029/2004GL021040>

Gulev, S. K., & Grigorieva, V. (2006). Variability of the winterwind waves and swell in the North Atlantic and North Pacific revealed by the voluntary observing ship data. *Journal of Climate*, 19, 5667–5685. <https://doi.org/10.1175/JCLI3936.1>

Hansom, J. D., Switzer, A. D., & Pile, J. (2015). Extreme waves: Causes, characteristics, and impact on coastal environments and society. In J. F. Shroder, J. T. Ellis, & D. J. Sherman (Eds.), *Coastal and marine hazards, risks, and disasters* (pp. 307–334). Elsevier. <https://doi.org/10.1016/B978-0-12-396483-0.00011-X>

Hemer, M. A., Church, J. A., & Hunter, J. R. (2010). Variability and trends in the directional wave climate of the Southern Hemisphere. *International Journal of Climatology*, 30, 475–491. <https://doi.org/10.1002/joc.1900>

Hemer, M. A., Fan, Y., Mori, N., Semedo, A., & Wang, X. L. (2013). Projected changes in wave climate from a multi-model ensemble. *Nature Climate Change*, 3, 471–476. <https://doi.org/10.1038/nclimate1791>

Hodges, K., Cobb, A., & Vidale, P. L. (2013). How well are tropical cyclones represented in reanalysis datasets? *Journal of Climate*, 30(14), 5243–5264. <https://doi.org/10.1175/JCLI-D-16-0557.1>

Hurrell, J. W. (1995). Decadal trends in the North Atlantic oscillation: Regional temperatures and precipitation. *Science*, 269, 676–679. <https://doi.org/10.1126/science.269.5224.676>

Hurrell, J. W., Kushnir, Y., Ottersen, G., & Visbeck, M. (2003). The North Atlantic oscillation: Climate significance and environmental impact. In J. W. Hurrell, Y. Kushnir, G. Ottersen, & M. Visbeck (Eds.), *Geophysical monograph series* (Vol. 134, p. 279). American Geophysical Union.

Hurrell, J. W., & Van Loon, H. (1997). Decadal variations in climate associated with the North Atlantic oscillation. *Climatic Change*, 36, 301–326. <https://doi.org/10.1023/A:1005314315270>

- Izaguirre, C., Méndez, F. J., Menéndez, M., & Losada, I. J. (2011). Global extreme wave height variability based on satellite data. *Geophysical Research Letters*, *38*, L10607. <https://doi.org/10.1029/2011GL047302>
- Izaguirre, C., Méndez, F. J., Menéndez, M., Luceño, A., & Losada, I. J. (2010). Extreme wave climate variability in southern Europe using satellite data. *Journal of Geophysical Research*, *115*, C04009. <https://doi.org/10.1029/2009JC005802>
- Jin, F. F., Boucharel, J., & Lin, I. I. (2014). Eastern Pacific tropical cyclones intensified by El Niño delivery of subsurface ocean heat. *Nature*, *516*(7529), 82–85. <https://doi.org/10.1038/nature13958>
- Kao, H. Y., & Yu, J. Y. (2009). Contrasting Eastern-Pacific and Central-Pacific types of ENSO. *Journal of Climate*, *22*(3), 615–632. <https://doi.org/10.1175/2008JCLI2309.1>
- Kharin, V. V., & Zwiers, F. W. (2005). Estimating extremes in transient climate change simulations. *Journal of Climate*, *18*, 1156–1173. <https://doi.org/10.1175/JCLI3320.1>
- Kuleshov, Y., Qi, L., Fawcett, R., & Jones, D. (2008). On tropical cyclone activity in the Southern Hemisphere: Trends and the ENSO connection. *Geophysical Research Letters*, *35*, L14S08. <https://doi.org/10.1029/2007GL032983>
- Kumar, P., Kaur, S., Weller, E., & Min, S.-K. (2019). Influence of natural climate variability on the extreme ocean surface wave heights over the Indian Ocean. *Journal of Geophysical Research: Oceans*, *124*, 6176–6199. <https://doi.org/10.1029/2019JC015391>
- Kumar, P., Min, S. K., Weller, E., Lee, H., & Wang, X. L. (2016). Influence of climate variability on extreme ocean surface wave heights assessed from ERA-interim and ERA-20C. *Journal of Climate*, *29*, 4031–4046. <https://doi.org/10.1175/JCLI-D-15-0580.1>
- Lau, N.-C. (1988). Variability of the observed midlatitude storm tracks in relation to low-frequency changes in the circulation pattern. *Journal of the Atmospheric Sciences*, *45*, 2718–2743. [https://doi.org/10.1175/1520-0469\(1988\)045<2718:votoms>2.0.co;2](https://doi.org/10.1175/1520-0469(1988)045<2718:votoms>2.0.co;2)
- Lim, E.-P., Hendon, H. H., Arblaster, J. M., Delage, F., Nguyen, H., Min, S.-K., & Wheeler, M. C. (2016). The impact of the Southern Annular Mode on future changes in Southern Hemisphere rainfall. *Geophysical Research Letters*, *43*, 7160–7167. <https://doi.org/10.1002/2016GL069453>
- Linkin, M. E., & Nigam, S. (2008). The North Pacific Oscillation-West Pacific teleconnection pattern: Mature-phase structure and winter impacts. *Journal of Climate*, *21*, 1979–1997. <https://doi.org/10.1175/2007JCLI2048.1>
- Marshall, G. J. (2003). Trends in the Southern Annular Mode from observations and reanalyses. *Journal of Climate*, *16*, 4134–4143. [https://doi.org/10.1175/1520-0442\(2003\)016<4134:TITSAM>2.0.CO;2](https://doi.org/10.1175/1520-0442(2003)016<4134:TITSAM>2.0.CO;2)
- Marshall, A. G., Hemer, M. A., Hendon, H. H., & McInnes, K. L. (2018). Southern annular mode impacts on global ocean surface waves. *Ocean Modelling*, *129*, 58–74. <https://doi.org/10.1016/j.ocemod.2018.07.007>
- Meneghini, B., Simmonds, I., & Smith, I. N. (2007). Association between Australian rainfall and the Southern Annular Mode. *International Journal of Climatology*, *27*, 109–121. <https://doi.org/10.1002/joc.1370>
- Menendez, M., Mendez, F. J., Losada, I. J., & Graham, N. E. (2008). Variability of extreme wave heights in the northeast Pacific Ocean based on buoy measurements. *Geophysical Research Letters*, *35*, L22607. <https://doi.org/10.1029/2008GL035394>
- Mentaschi, L., Vousdoukas, M. I., Voukouvalas, E., Dosio, A., & Feyen, L. (2017). Global changes of extreme coastal wave energy fluxes triggered by intensified teleconnection patterns. *Geophysical Research Letters*, *44*, 2416–2426. <https://doi.org/10.1002/2016GL072488>
- Min, S.-K., Cai, W., & Whetton, P. (2013). Influence of climate variability on seasonal extremes over Australia. *Journal of Geophysical Research: Atmospheres*, *118*, 643–654. <https://doi.org/10.1002/jgrd.50164>
- Mo, K. C., & Paegle, J. N. (2001). The Pacific-South American modes and their downstream effects. *International Journal of Climatology*, *21*, 1211–1229. <https://doi.org/10.1002/joc.685>
- Mori, N., Yasuda, T., Mase, H., Tom, T., & Oku, Y. (2010). Projection of extreme wave climate change under global warming. *Hydrological Research Letters*, *4*, 15–19. <https://doi.org/10.3178/hrl.4.15>
- Paik, S., Min, S.-K., Kim, Y.-H., Kim, B.-M., Shioyama, H., & Heo, J. (2017). Attributing causes of 2015 record minimum sea-ice extent in the Sea of Okhotsk. *Journal of Climate*, *30*, 4693–4703. <https://doi.org/10.1175/JCLI-D-16-0587.1>
- Patra, A., & Bhaskaran, P. K. (2016). Trends in wind-wave climate over the head Bay of Bengal region. *International Journal of Climatology*, *36*, 4222–4240. <https://doi.org/10.1002/joc.4627>
- Patra, A., & Bhaskaran, P. K. (2017). Temporal variability in wind-wave climate and its validation with ESSO-NIOT wave atlas for the head Bay of Bengal. *Climate Dynamics*, *49*, 1271–1288. <https://doi.org/10.1007/s00382-016-3385-z>
- Power, S., Casey, T., Folland, C., Colman, A., & Mehta, V. (1999). Inter-decadal modulation of the impact of ENSO on Australia. *Climate Dynamics*, *15*(5), 319–324. <https://doi.org/10.1007/s003820050284>
- Queffelec, P., & Croizé-Fillon, D. (2017). *Global altimeter SWH data set*. User Guide, Laboratoire d’Océanographie Spatiale, Ifremer, February 2017. Retrieved from [ftp://ftp.ifremer.fr/ifremer/cersat/products/swath/altimeters/waves/documentation/altimeter\\_wave\\_merge\\_\\_11.4.pdf](ftp://ftp.ifremer.fr/ifremer/cersat/products/swath/altimeters/waves/documentation/altimeter_wave_merge__11.4.pdf)
- Rasmusson, E. M., & Carpenter, T. H. (1982). Variations in tropical sea surface temperature and surface wind fields associated with the Southern Oscillation/El Niño. *Monthly Weather Review*, *110*, 1103–1113. [https://doi.org/10.1175/1520-0493\(1982\)110<0354:VITSST>2.0.CO;2](https://doi.org/10.1175/1520-0493(1982)110<0354:VITSST>2.0.CO;2)
- Reguero, B. G., Losada, I. J., & Méndez, F. J. (2019). A recent increase in global wave power as a consequence of oceanic warming. *Nature Communications*, *10*, 1–14. <https://doi.org/10.1038/s41467-018-08066-0>
- Rogers, J. C. (1981). The North Pacific Oscillation. *Journal of Climatology*, *1*, 39–57. <https://doi.org/10.1002/joc.3370010106>
- Santo, H., Taylor, P. H., Woollings, T., & Poulson, S. (2015). Decadal wave power variability in the North-East Atlantic and North Sea. *Geophysical Research Letters*, *42*, 4956–4963. <https://doi.org/10.1002/2015GL064488>
- Semedo, A., Sušelj, K., Rutgersson, A., & Sterl, A. (2011). A global view on the wind sea and swell climate and variability from ERA-40. *Journal of Climate*, *24*, 1461–1479. <https://doi.org/10.1175/2010JCLI3718.1>
- Stopa, J. E., Cheung, K. F., Tolman, H. L., & Chawla, A. (2013). Patterns and cycles in the Climate Forecast System Reanalysis wind and wave data. *Ocean Modelling*, *70*, 207–220. <https://doi.org/10.1016/j.ocemod.2012.10.005>
- Takbash, A., Young, I. R., & Breivik, O. (2019). Global wind speed and wave height extremes derived from long-duration satellite records. *Journal of Climate*, *32*, 109–126. <https://doi.org/10.1175/JCLI-D-18-0520.1>
- Vincent, E. M., Lengaigne, M., Menkes, C. E., Jourdain, N. C., Marchesio, P., & Madec, G. (2011). Interannual variability of the South Pacific Convergence Zone and implications for tropical cyclone genesis. *Climate Dynamics*, *36*, 1881–1896. <https://doi.org/10.1007/s00382-009-0716-3>
- Wang, X. L., Feng, Y., & Swail, V. R. (2012). North Atlantic wave height trends as reconstructed from the 20th century reanalysis. *Geophysical Research Letters*, *39*, L18705. <https://doi.org/10.1029/2012GL053381>
- Wang, X. L., & Swail, V. R. (2001). Changes of extreme wave heights in Northern Hemisphere oceans and related atmospheric circulation regimes. *Journal of Climate*, *14*, 2204–2221. [https://doi.org/10.1175/1520-0442\(2001\)014<2204:COEWHI.2.0.CO;2](https://doi.org/10.1175/1520-0442(2001)014<2204:COEWHI.2.0.CO;2)

- Wang, X. L., & Swail, V. R. (2002). Trends of Atlantic wave extremes as simulated in a 40-yr wave hindcast using kinematically reanalyzed wind fields. *Journal of Climate*, *15*, 1020–1035. [https://doi.org/10.1175/1520-0442\(2002\)015<1020:TOAWEA>2.0.CO;2](https://doi.org/10.1175/1520-0442(2002)015<1020:TOAWEA>2.0.CO;2)
- Wang, B., Wu, R., & Fu, X. (2000). Pacific-East Asian teleconnection: How does ENSO affect East Asian climate? *Journal of Climate*, *13*, 1517–1536. [https://doi.org/10.1175/1520-0442\(2000\)013<1517:PEATHD>2.0.CO;2](https://doi.org/10.1175/1520-0442(2000)013<1517:PEATHD>2.0.CO;2)
- Wang, B., & Zhang, Q. (2002). Pacific-East Asian teleconnection. Part II: How the Philippine Sea anomalous anticyclone is established during El Niño development. *Journal of Climate*, *15*, 3252–3265. [https://doi.org/10.1175/1520-0442\(2002\)015<3252:PEATPI>2.0.CO;2](https://doi.org/10.1175/1520-0442(2002)015<3252:PEATPI>2.0.CO;2)
- Wolter, K., & Timlin, M. S. (2011). El Niño/Southern Oscillation behaviour since 1871 as diagnosed in an extended multivariate ENSO index (MEI.ext). *International Journal of Climatology*, *31*, 1074–1087. <https://doi.org/10.1002/joc.2336>
- Yeh, S.-W., Cai, W., Min, S.-K., McPhaden, M. J., Dommenges, D., Dewitte, B., et al. (2018). ENSO atmospheric teleconnections and their response to greenhouse gas forcing. *Reviews of Geophysics*, *56*, 185–206. <https://doi.org/10.1002/2017RG000568>
- Yeh, S.-W., Yi, D.-W., Sung, M.-K., & Kim, Y.-H. (2018). An eastward shift of the North Pacific Oscillation after the mid-1990s and its relationship with ENSO. *Geophysical Research Letters*, *45*, 6654–6660. <https://doi.org/10.1029/2018GL078671>
- Young, I. R. (1999). Seasonal variability of the global ocean wind and wave climate. *International Journal of Climatology*, *19*, 931–950. [https://doi.org/10.1002/\(SICI\)1097-0088\(199907\)19:9:931::AID-JOC412.3.O.CO;2-O](https://doi.org/10.1002/(SICI)1097-0088(199907)19:9:931::AID-JOC412.3.O.CO;2-O)
- Young, I. R., & Ribal, A. (2019). Multiplatform evaluation of global trends in wind speed and wave height. *Science*, *364*, 548–552. <https://doi.org/10.1126/science.aav9527>
- Young, I. R., Vinoth, J., Zieger, S., & Babanin, A. V. (2012). Investigation of trends in extreme value wave height and wind speed. *Journal of Geophysical Research: Oceans*, *117*, 1–13. <https://doi.org/10.1029/2011JC007753>
- Young, I. R., Zieger, S., & Babanin, A. V. (2011). Global trends in wind speed and wave height. *Science*, *332*, 451–455. <https://doi.org/10.1126/science.1197219>
- Yu, J. Y., Kao, H. Y., Lee, T., & Kim, S. T. (2011). Subsurface ocean temperature indices for Central-Pacific and Eastern-Pacific types of El Niño and La Niña events. *Theoretical and Applied Climatology*, *103*, 337–344. <https://doi.org/10.1007/s00704-010-0307-6>
- Zhang, X. B., Wang, J. F., Zwiers, F. W., & Groisman, P. Y. (2010). The influence of large-scale climate variability on winter maximum daily precipitation over North America. *Journal of Climate*, *23*, 2901–2915. <https://doi.org/10.1175/2010JCLI3249.1>